SHIELD: Skull-shaped hemispheric implants enabling large-scale-electrophysiology datasets in the mouse brain

Corbett Bennett[1,3], Ben Ouellette[1], Tamina K Ramirez[1], Alex Cahoon, Hannah Cabasco, Hannah Belski, Ryan Gillis, Conor Grasso, Robert Howard, Tye Johnson, Henry Loeffler, Heston Smith, David Sullivan, Allison Williford, Shiella Caldejon, Severine Durand, Samuel Gale, Alan Guthrie, Vivian Ha, Warren Han, Ben Hardcastle, Ethan McBride, Chris Mochizuki, Arjun Sridhar, Lucas Suarez, Jackie Swapp, Joshua Wilkes, Colin Farrell, Peter A. Groblewski[2,3], Shawn R Olsen[2,3]

[1] Equal contributors
[2] Co-senior authors
[3] Corresponding authors
Email: corbettb@alleninstitute.org, peterg@alleninstitute.org, shawno@alleninstitute.org

Allen Institute, Seattle WA 98109

Summary

To understand the neural basis of behavior, it is essential to measure spiking dynamics across many interacting brain regions. While new technology, such as Neuropixels probes, facilitates multi-regional recordings, significant surgical and procedural hurdles remain for these experiments to achieve their full potential. Here, we describe a novel 3D-printed cranial implant for electrophysiological recordings from distributed areas of the mouse brain. The skull-shaped implant is designed with customizable insertion holes, allowing targeting of dozens of cortical and subcortical structures in single mice. We demonstrate the procedure's high success rate, implant biocompatibility, lack of adverse effects on behavior training, compatibility with optical imaging and optogenetics, and repeated high-quality Neuropixels recordings over multiple days. To showcase the scientific utility of this new methodology, we use multi-probe recordings to reveal how alpha rhythms organize spiking activity across visual and sensorimotor networks. Overall, this methodology enables powerful large-scale electrophysiological measurements for the study of distributed computation in the mouse brain.

Highlights

- Novel cranial implant and surgical methods for distributed recordings with multiple Neuropixels probes in the mouse brain
- Customizable 3D-printed implants provide flexible access to brain-wide targets and are compatible with optical imaging and optogenetics
- Preparation remains viable over multiple days, allowing repeated recordings to maximize yield from single animals
- Multi-probe recordings in behaving mice reveal how alpha-like oscillations organize spiking activity across distributed visual and sensorimotor networks

In Brief

High-density electrode arrays such as Neuropixels are transformative for neuroscience research, but optimized surgical and experimental methodologies are necessary to fully harness the power of these devices. Here, Bennett et al. describe customizable cranial implants and workflows for multi-probe recordings of neuronal spiking across the mouse brain.

INTRODUCTION

The neural mechanisms mediating behavioral and cognitive operations in the mammalian brain involve coordinated activity dynamics across highly distributed cortical and subcortical networks. Even simple sensorimotor transformations engage dozens of brain regions working in concert to convert sensory input into decisions and motor actions (Guo et al., 2014; Inagaki et al., 2022; Romo and Salinas, 2003). The neural dynamics underlying these transformations have traditionally been studied one region at a time, however, technical advances have opened new avenues for multi-regional measurement of neural activity (Machado et al., 2022). This is particularly true in the mouse, where new high-channel-count electrophysiology and large-scale calcium imaging have flourished. For instance, calcium imaging methods can survey activity across most of the dorsal cortex (Allen et al., 2019; Cardin et al., 2020; Musall et al., 2019; Ren and Komiyama, 2021; Wekselblatt et al., 2016), including large field of view 2-photon microscopes that provide neuron-level resolution over millimeter scales (Kim et al., 2016; Sofroniew et al., 2016). However, calcium imaging is unable to capture single spikes and fast activity dynamics in neural networks, and subcortical brain regions are less accessible, typically requiring the removal of overlying brain tissue, such as with implanted GRIN lenses (Jung et al., 2004). In contrast, extracellular electrophysiology using multiple high-density probes, such as Neuropixels, provides the opportunity to record from distributed cortical and subcortical brain regions with high temporal fidelity and single spike resolution (Jun et al., 2017).

Multi-Neuropixels recordings have been used in mice to simultaneously record from 2-8 independently inserted probes (Chen et al., 2023; IBL et al., 2022; McBride et al., 2023; Peters et al., 2021; Siegle et al., 2021; Steinmetz et al., 2019; Stringer et al., 2019; Vesuna et al., 2020). These experiments are technically demanding, in part due to the challenge of accessing many brain regions in the same animal. Most previous studies have addressed this challenge by making multiple small craniotomies (~1mm) or burr-holes through which individual probes are inserted to target brain regions of interest (Figure 1A). For example, this technique has been used to record with 8 probes during spontaneous activity in awake mice (Stringer et al., 2019), 2-3 probes during a visual decision-making task (IBL et al., 2022; Steinmetz et al., 2019), 4 probes during dissociative drug administration (Vesuna et al., 2020), and up to 5 probes during a memory-guided movement task (Chen et al., 2023). Though creating multiple small craniotomies is a straightforward and flexible surgical procedure, there are several drawbacks to this method. First, the craniotomy is typically performed on the day of recording and requires the mouse to be anesthetized. Mice are allowed to recover for a few hours before recording, but same-day anesthesia could alter natural neural dynamics and behavior (Bekhbat et al., 2016; Jacobsen et al., 2012; McKinney et al., 2022). Second, craniotomies can damage the underlying cortical tissue and, even in cases where no overt tissue damage occurs, can recruit a widespread neuroinflammatory response that persists for several weeks (Holtmaat et al., 2009). Third, performing many craniotomies is time-consuming, and the risk of brain damage and adverse effects of exposure to anesthesia increases with the number of craniotomies, putting a practical limit on the number of regions that can be targeted in a single experiment. Lastly, although recordings are often performed from the same mouse for multiple days, acute daily craniotomies can lead to infections and compromised brain health.

In our previous work, we developed an approach for accessing visual cortical regions of the mouse brain that employs an “insertion window” (Durand et al., 2022; Siegle et al., 2021). In this procedure, multiple probes are inserted into a large (5 mm) craniotomy centered on the primary

visual cortex. To stabilize the brain, a plastic window with insertion holes for each probe is installed before the recording, and the space between the window and the brain is filled with agar. This technique enabled us to obtain high-quality, stable 6-probe recordings from precisely identified visual areas in over a hundred mice (Durand et al., 2022; Siegle et al., 2021). However, the procedure was developed for one or two acute recordings per animal, and probe insertions were limited to regions lying within the cranial window.

To measure spiking activity across the mouse brain, we sought to develop a new procedure that would meet the following requirements: 1) provide flexible access to a broad set of brain areas, 2) facilitate simultaneous multi-probe recordings, 3) maintain brain health for many recording days, and 4) provide optical access to the dorsal brain surface. We considered several approaches and assessed the techniques used in previous studies (Figure 1A) (Chen et al., 2023; IBL et al., 2022; Steinmetz et al., 2019; Stringer et al., 2019; Vesuna et al., 2020). Due to the drawbacks enumerated above, we sought alternatives to the multiple small craniotomy approach. Another possibility was to implant several insertion windows over the regions of interest; for instance, one insertion window over visual cortical areas and one window over frontal cortical areas (Figure 1A). This approach would allow access to distributed brain regions without the need for day-of craniotomies but would lack flexibility, since each recording configuration would require a separate set of craniotomies, and many window positions would be mutually incompatible.

Thus, to meet our requirements, we developed a novel cranial implant and surgical workflow called SHIELD (Skull-shaped Hemispheric Implants Enabling Large-scale-electrophysiology Datasets), which permits highly distributed and repeated recordings across the mouse brain. Our approach was inspired by prior methods in which a large fraction of the mouse skull is replaced with a window or surrogate skull for optical imaging (Allen et al., 2017; Ghanbari et al., 2019; Kim et al., 2016; Wekselblatt et al., 2016). Here, we describe a workflow wherein a wide range of target brain locations can be accessed for silicon probe recordings via a 3D-printed skull implant. The preparation allows for sequential multi-day recordings with many flexible probe insertions in a single mouse (Figure 1B). Moreover, the implant is transparent, allowing optical imaging, optogenetic perturbations, and optotagging to identify genetically defined subsets of neurons. Finally, we demonstrate the power of the SHIELD methodology during head-fixed behavioral experiments (Figure 1C) to reveal how alpha brain oscillations organize functional spiking interactions across distributed visual and sensorimotor networks.

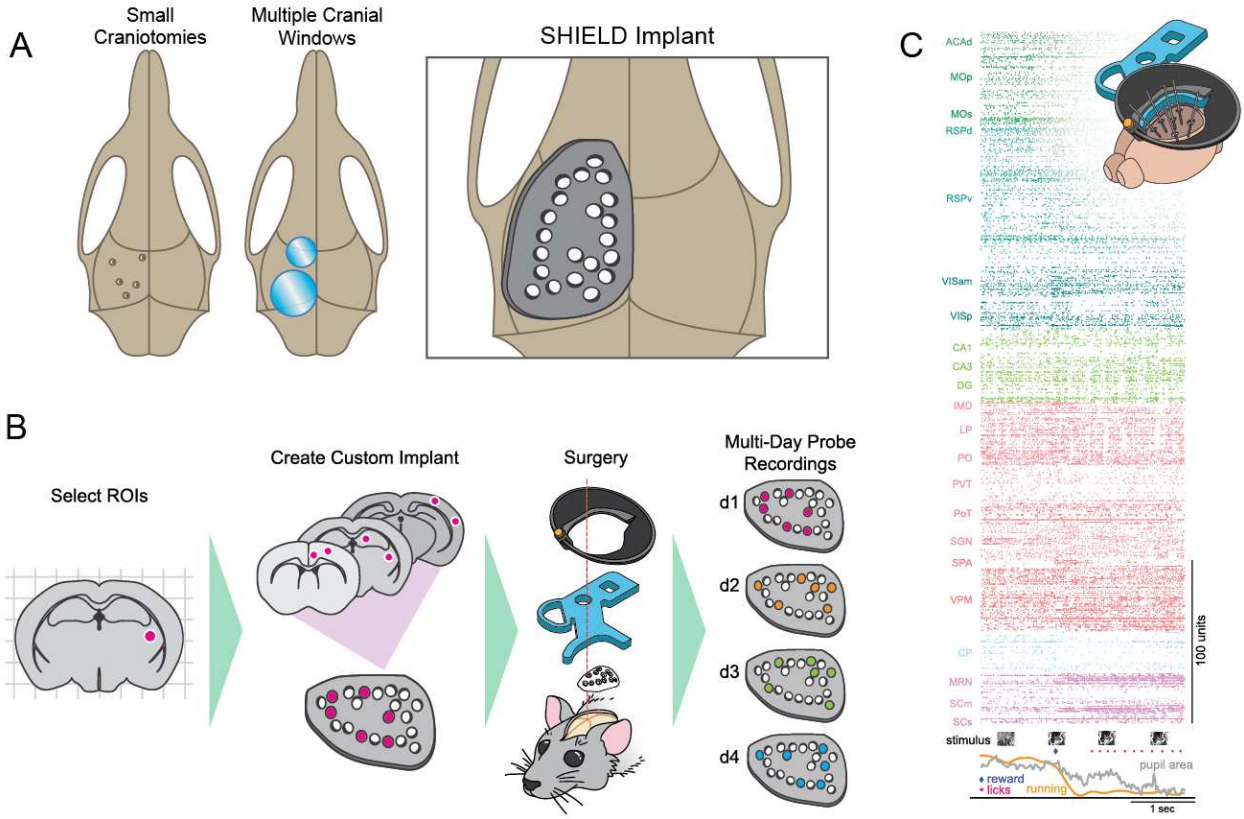

Figure 1 | Overview of implant and brain targeting strategy. A) Approaches for accessing the brain to insert Neuropixels probes. **B)** Workflow for creating SHIELD implant to target distributed cortical and subcortical regions. **C)** Raster plot showing spiking of 865 units across 22 areas in one example recording. During recording, the mouse performed a visual change detection task. Task-related behavioral data are aligned to a stimulus change after which the mouse licked to consume a water reward.

RESULTS

Design and 3D-printing of hemispheric skull implant

We sought to design a cranial implant that would fit mice within our surgical age range (postnatal day 56 ± 9; mean ± std). To conform the implant to the curvature of the mouse brain, we first performed cranial contour mapping in eight mice (Figure 2A). We then used CAD modeling to generate an ellipsoid shape that encompassed the set of skull contours (Figure 2A). This ellipsoid, defined by three curves with respect to bregma (Figure S1A), was the starting point for engineering the custom implants. Stereotaxic targets were selected for each probe to determine hole locations, and the orientation of each probe relative to bregma was used to calculate the necessary insertion point on the surface of the implant (Figure 2B). Small insertion holes (0.75-1 mm) were then made in the implant CAD model at these locations (Figure S1C). In this study, we generated four distinct implants with 13-21 holes distributed broadly over the surface of the implant (Figure 2B). To facilitate angled probe insertions, the upper surface of the hole is designed with symmetrical sloping cutaways (chamfers) (Figure 2B). To provide a gluing surface to attach the implant to the skull, a flange (250 µm thick) extends 600 µm beyond the cranial window. The inner part of the implant, circumscribed by this flange, extends 400 µm down into the craniotomy

and sits on the brain surface (Figure S1A). Once complete, the implant CAD files are imported into Formlabs PreForm™ software and printed on a Formlabs Form 3+ printer using clear resin at 25 µm layer height. After printing, the implants are washed in an isopropyl alcohol bath (Formlabs Wash Station) maintained at 99% concentration for 10 minutes (Figure 2B) and then UV cured in the Formlabs Cure station at 60°C for 15 minutes.

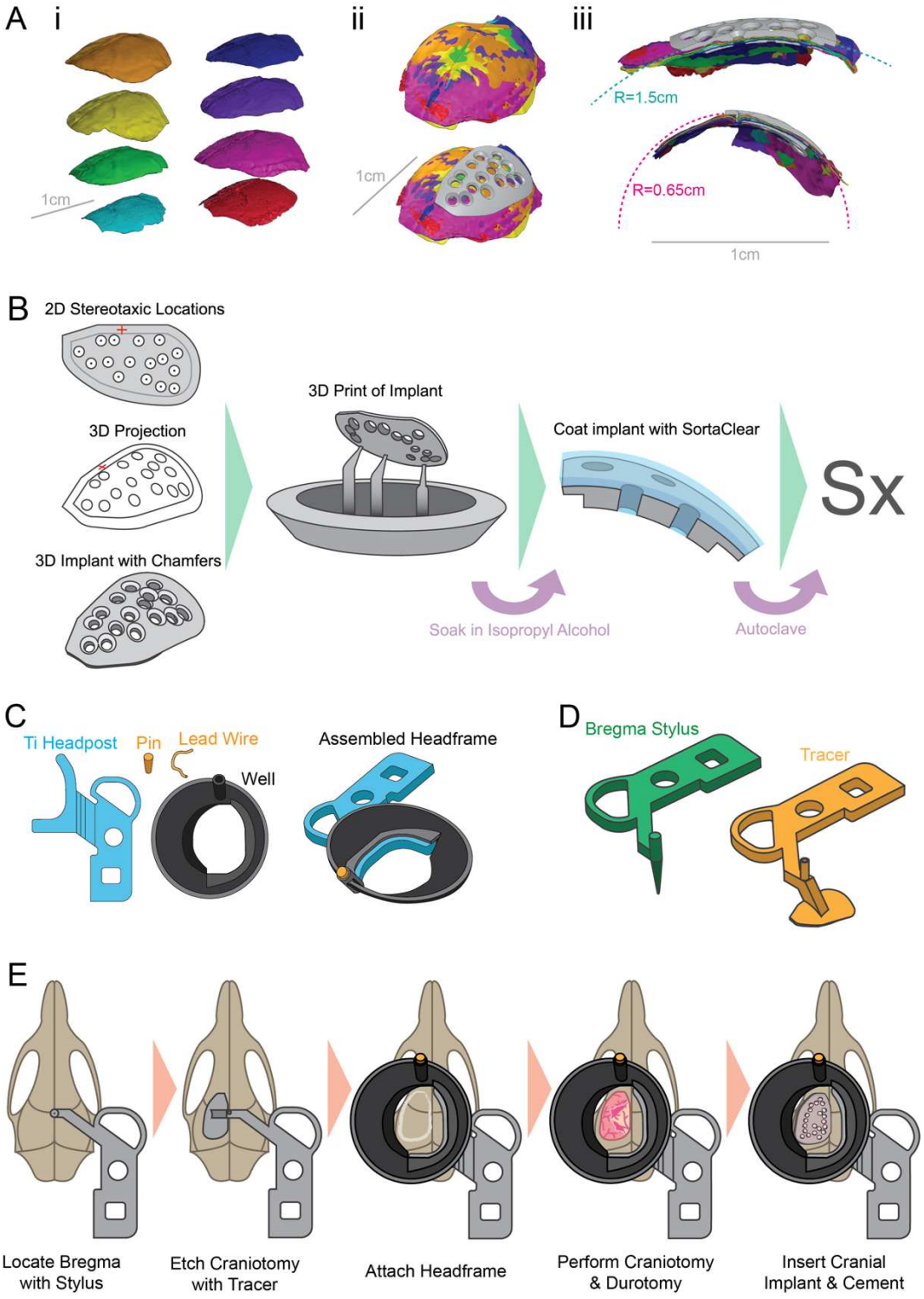

Figure 2 | Design, preparation and surgical installation of SHIELD implant. A) (i) Cranial contours obtained with laser scanning from eight mice, **(ii)** bregma-aligned composite contour with implant overlaid, and **(iii)** sagittal and coronal cross sections of implant overlays. **B)** Workflow for creating and preparing 3D-printed cranial implant. The set of desired insertion holes are defined in CAD software and chamfers are added. The implant is 3D-printed, cleaned, coated with SORTA-Clear, and then autoclaved. **C)** The headframe assembly includes a 3D-printed titanium headplate mated with a plastic well that includes a gold pin and silver wire. **D)** Custom tooling for locating bregma and tracing the outline of the craniotomy. **E)** Schematized view of the surgical workflow.

Installation of SHIELD implant and quality control evaluation

Before surgically installing the cranial implant, SORTA-Clear 18™ (Smooth-On) silicone rubber is applied to fill each insertion hole and form a thin layer on the implant's dorsal surface (Figure 2B and Figure S1D). This layer of SORTA-Clear provides a solid substrate that plugs the holes prior to recordings while maintaining the optical transparency necessary for regular brain health evaluations and through-implant imaging. The coated implants are then autoclaved at a temperature of 131°C and a pressure of 14.7 psi for 5 minutes. Note that autoclaving at higher temperatures can lead to defects in the implant.

To install the implant, mice are anesthetized and placed in a stereotaxic frame. The dorsal scalp is removed, the skull leveled, and bregma located using tooling adapted from a previously described headframe and clamping system (Groblewski et al., 2020b). Bregma serves as a reference point for accurate placement of both the implant and the headframe. An outline of the implant location is etched using a custom tracing tool (Figure 2D,E), and the assembled headframe (Figure 2C) is cemented in place. A craniotomy is performed using the traced implant shape as a guide, and the prepared 3D-printed implant is placed in the opening (Figure 2E). The edges of the implant are sealed to the skull using a light cure adhesive (Loctite 4305) and further reinforced with dental cement. Finally, a removable plastic cap is placed over the well to protect the implant's silicone coating from cage debris.

We performed extensive work to optimize the quality and reproducibility of the SHIELD methodology and describe several key tips here (Figure S2). Care should be taken when drilling near veins and sinuses; in particular, the anterior-lateral portion of the drill path comes near the rostral rhinal vein and the dense vasculature around the sagittal sinus (Figure S2A). Our implant shape has been designed in part to minimize drilling in this area, which can cause excessive bleeding. Do not over-drill anywhere along the drill path, as this can damage the underlying brain (Figure S2E). Generally, a very small but continuous crack in the final layer of skull is sufficient to achieve good separation. In addition, it is advised to keep a thin layer of bone along the lateral edge of the craniotomy (Figure S2B); this serves as a hinge and facilitates removal of the bone flap with fine forceps starting on the medial side (Figure S2C). To perform the durotomy, make an incision along the anterior-posterior axis with a durotomy probe (Fine Science Tools), then cut the dura around the perimeter of the craniotomy using 45° Vannas scissors. The dura should be cleanly removed without tearing to avoid damaging underlying tissue or rupturing attached blood vessels along the midline (Figure S2F). The implant should be carefully aligned during placement using the anterior and medial edges of the craniotomy as reference points (Figure S2D). Improper seating of the implant into the craniotomy can lead to brain deformation (Figure S2G).

To validate the integrity, health, and function of the brain following the SHIELD implant surgery, we performed a series of evaluations. First, we took images of the brain at multiple timepoints following the implant surgery. The transparent implant allowed for visual inspection of

abnormalities, including bleeding, tissue damage, bruising, and implant clarity over eight weeks (Figure 3A). Of the 106 mice entering surgery for this study, 79 passed all quality checks with no issues, 14 passed with a flag that eventually resolved, and 13 mice failed (Figure 3B; Methods). The resulting passing rate of 87.7% is on par with the success rate for our previously used 5 mm cranial window surgery for Neuropixels recordings (90%; 122/135 mice) (Durand et al., 2022; Siegle et al., 2021).

Next, we sought to characterize the functional integrity of the brain at the mesoscale level. We tested whether we could perform intrinsic signal imaging (ISI) through the implant to generate functional maps of the visual cortical areas using procedures previously developed for imaging through a glass window (de Vries et al., 2020; Siegle et al., 2021). We found that standard procedures successfully mapped the retinotopic boundaries of V1 and many higher visual cortical areas (Figure 3C). These results show that 1) the optical clarity of the cranial implant is sufficient for functional imaging, and 2) the functional properties and underlying organization of the visual cortical areas remain intact following the surgical procedure.

We also performed histological analysis to evaluate whether the implant caused a neuroinflammatory response triggered by injury to the brain. We examined whether the brains of implanted mice showed activation of glial fibrillary acidic protein (GFAP), a widely used marker of neuroinflammation (Eng and Ghirnikar, 1994; Yang and Wang, 2015). We compared GFAP levels on the implanted left hemisphere to the unaltered right hemisphere and found little evidence of GFAP activation or cell loss (visualized with DAPI and NeuN), indicating that the implant did not compromise the health of underlying tissue (Figure. 3D; n=10 mice, 56±12 days post surgery; mean±stdev).

Finally, we assessed the effect of the SHIELD implant on mouse behavior. Implanted animals did not display gross changes in home cage behavior and demonstrated similar or faster learning rates on a visually-guided behavioral task compared to mice with the 5 mm visual cortex cranial window implant used in previous studies (Figure 3E) (Garrett et al., 2023; Groblewski et al., 2020a).

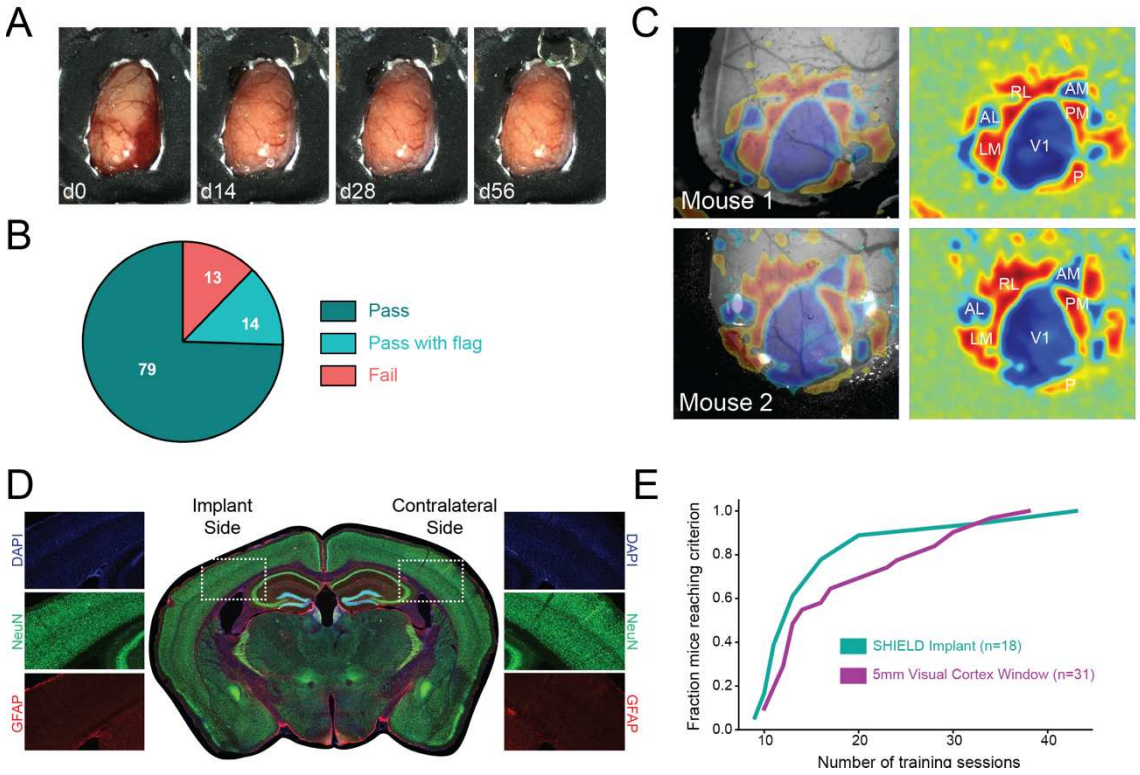

Figure 3 | SHIELD procedure preserves the health and function of underlying brain. A) Longitudinal images of the cranial implant from a single mouse. **B)** Surgical outcomes from 106 cranial implant surgeries performed over one year. **C)** Functional boundaries of the visual cortex mapped through the implant using intrinsic signal imaging. Left, visual sign map overlaid on implant. Right, sign map with visual area labels. **D)** Histology following cranial implant surgery shows lack of neuronal loss (DAPI, NeuN) and absence of GFAP activation. **E)** Compared to mice implanted with a 5mm visual cortex window, mice with hemispheric implants show similar (or faster) learning rates on a visually-guided behavioral task.

High-quality multi-Neuropixels recordings

After successful installation of the SHIELD implant, mice in our study underwent behavioral training for 3-5 weeks before multi-probe recordings were performed. During this time, the cranial implant remained covered with SORTA-Clear silicone plugs. Since Neuropixels probes cannot penetrate this durable silicone, it is removed prior to recording and replaced with a temporary Kwik-cast plug. On the recording day, this plug is removed and the implant is covered with agar for mechanical stability (Figure 4A). The probes (each mounted on an independent micromanipulator) are then driven to their respective insertion hole and slowly inserted through the agar into the brain (Figure 4A). Depending on the target structure, the probes are inserted to depths between 2-4 mm. Between daily experimental sessions, the agar covering the implant is gently removed and replaced with a layer of Kwik-cast (Figure 4A).

In a typical 6 probe experimental session, we recorded activity from over 1,800 units spanning ~25 brain areas (1821 ± 341.9 units; 28.1 ± 5.1 areas, mean ± std; Figure 4B). Across mice, insertions belonging to the same probe trajectory, defined by the probe orientation and the implant hole through which it was inserted, entered the brain at similar locations after post-hoc registration to the Allen Common Coordinate Framework (CCF), (n = 15 trajectories, median absolute deviation in CCF brain insertion coordinates: 150 μm in the medial-lateral axis, 200 μm in the

anterior-posterior axis; median across trajectories; Figure 4B). Thus, our procedure allows users to consistently target areas of interest across animals with a dispersion of only ~250 μm (a fraction of the 0.75 mm hole diameter).

A critical feature of extracellular electrophysiological recordings is the mechanical stability of the probe relative to the brain, since this can impact the fidelity of spike sorting and the ability to track neurons over the recording session – a factor that is particularly vital for recordings in behaving mice. Thus, it is important to assess the quality of recordings during an active behavioral task. In our experiments mice were head-fixed, but free to run on a disc while they performed a visual behavioral task requiring licking to report perception of target stimuli. Despite these possible sources of brain motion, we found recordings were highly stable, as demonstrated by 'drift maps' that track the depth of each recorded unit on the probe over the duration of the experimental session (Figure 4C). We rarely observed discontinuous or abrupt shifts in the depth of units in the drift map. In addition, spike waveform shapes of individual units remained consistent over the course of the recording (Figure 4C). We quantified the drift of each unit in these experiments and found it was only slightly higher than that observed in our previous recordings using the 5 mm insertion window method (SHIELD: 25.1 ± 0.1 μm, 5 mm window: 22.82 ± 0.05; median ± sem; Figure 4D) (Durand et al., 2022; Siegle et al., 2021).

To further evaluate the recordings, we computed a battery of additional unit-level quality control (QC) metrics for experiments performed with the SHIELD implant as well as our previously used 5 mm visual cortex window recordings. This battery included metrics to evaluate unit stability and signal-to-noise ('presence ratio', 'amplitude cutoff', 'snr') as well as contamination from other units ('isi violations', 'isolation distance') (Siegle et al., 2021). Across all experiments, we found that the distribution of QC metrics was comparable between both surgical preparations (Figure 4D). Indeed, we found that the percentage of units passing our standard quality metric filter (see Methods) was very similar for the SHIELD versus 5 mm window implants (% units passing quality metrics criteria: SHIELD: 41.1, 5 mm window: 40.7).

Next, we sought to validate the functional properties of neurons measured using the SHIELD implant. To do this, we focused on visually-evoked activity in the primary visual cortex. In each of the four consecutive recording days, we measured many individual units with well-defined spatial receptive fields (Figure 4E). On successive days we inserted the probe into a nearby yet shifted location; the region of visual space preferred on each day matched the expected location indicated by the ISI-based retinotopic map. In addition, the stimulus-evoked temporal dynamics were highly similar across the four recording days (Figure 4F).

On each recording day, we measured the activity of nearly 300 units from each probe (Figure 4G). Unit yield was not significantly different across recording days ($p=0.21$ Kruskal-Wallis H-test). Additionally, the average firing rate of recorded units was similar across days ($p=0.21$ Kruskal-Wallis H-test), as was the fraction of VISp units that were significantly modulated by the receptive field-mapping stimulus ($p=0.38$ Kruskal-Wallis H-test). Together, these data provide additional confirmation that the brain remains healthy and stable over multiple days of consecutive recordings.

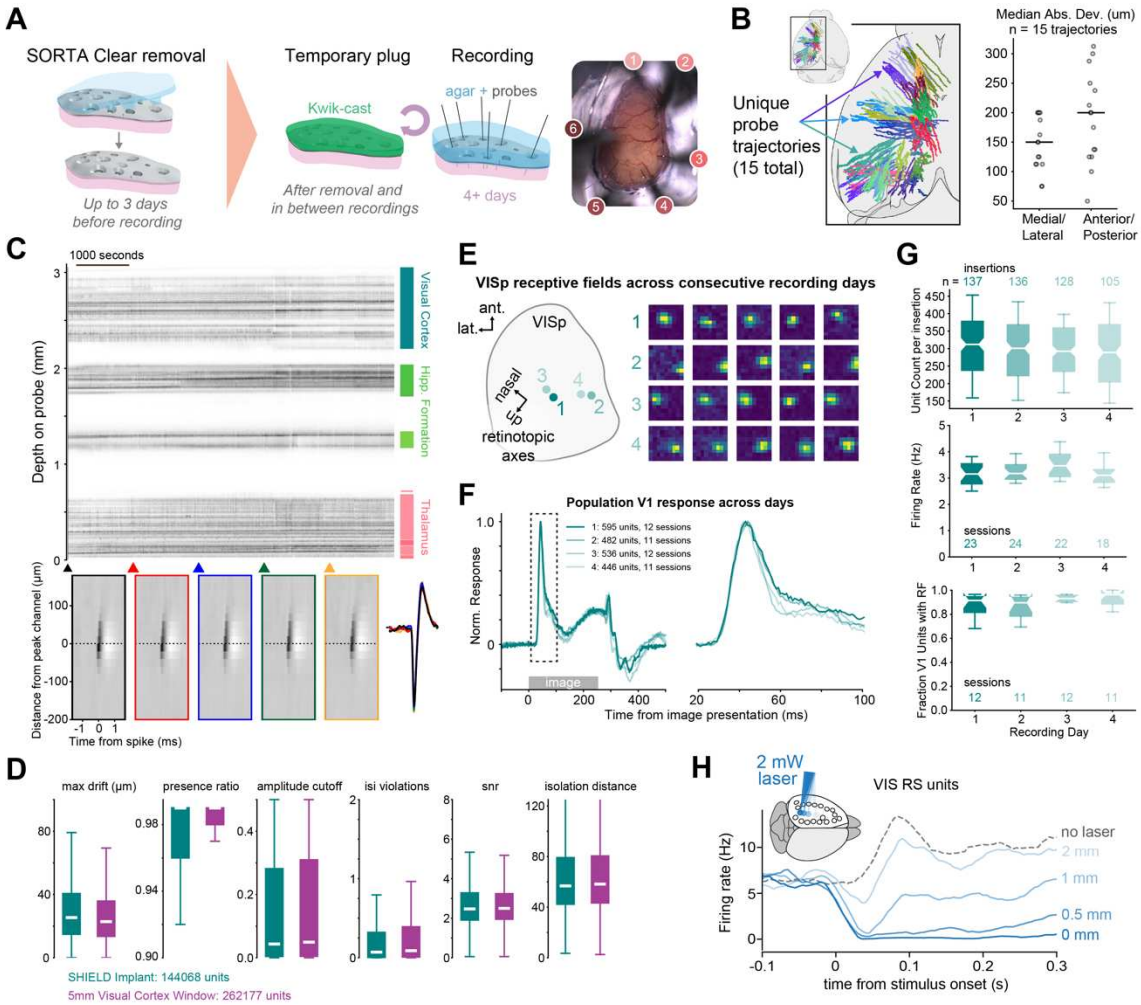

Figure 4. High-quality multi-Neuropixels recordings. A) Workflow for electrophysiological recordings. First, the SORTA-Clear covering that shielded the brain during behavior training is removed (up to 3 days prior to recording) and replaced with a temporary Kwik-cast plug. On the day of recording, this plug is removed and replaced with agar and a layer of silicone oil. After recording, the agar is removed and replaced with fresh Kwik-cast. **B)** (Left) Schematic of all probe insertion locations from this study registered to the CCF. Tracks are colored by insertion trajectory, as defined by the probe orientation and implant hole location. 15 unique insertion trajectories were examined in this study. (Right) The median absolute deviation in the medial-lateral and anterior-posterior axes across multiple insertions for each trajectory shown in (B). **C)** (Top) Drift map showing spiking activity across one probe during an example experiment. Darker dots indicate spikes with larger amplitude. (Bottom) Mean waveforms computed for five epochs across the recording duration for an example visual cortical unit to show waveform consistency. Arrowheads indicate the beginning of each epoch. The peak-channel waveform for all epochs are overlaid on the right. **D)** Unit quality metrics computed for this dataset (SHIELD implant) and the publicly available Allen Institute Neuropixels Visual Behavior dataset (5 mm window) for comparison. White band indicates median. Whiskers span the 10th and 90th percentiles. **E)** Example receptive fields from one mouse across four consecutive recording days. Recording locations within VISp are diagrammed on the left. Axes indicate known retinotopic gradients for azimuth (nasal/temporal) and elevation (up/down). **F)** Mean population visual responses to one image across four consecutive recording days. **G)** Functional unit properties across recording days. (Top) Unit count per probe insertion. (Middle) Overall session firing rate. (Bottom) Fraction of VISp units with significant receptive fields. Box plot notches indicate estimated 95% CI for median. **H)**

Efficacy of optogenetic silencing of cortex (VISp) in a VGAT-ChR2 mouse. The trace intensity indicates the distance of the laser spot from the recording location.

Next, we tested the ability to perform optogenetic inactivation of cortical activity through the implant. For this, we made recordings in VGAT-ChR2 mice, which express channelrhodopsin in all inhibitory interneurons in the cortex (Zhao et al., 2011). Activation of these interneurons produces potent network silencing with fast temporal dynamics (Guo et al., 2014; Li et al., 2019; Resulaj et al., 2018). Using a galvo-based laser delivery system, we shined blue light (488 nm) on the implant, systematically increasing the distance between the light and probe (0, 0.5, 1, 2 mm). During optogenetics we presented the animal with windowed grating stimuli (diameter: 50 degrees, duration: 250 ms) to verify that stimulus-evoked activity could be suppressed. The activity of regular spiking units (RS) in VISp was nearly completely silenced when the light was targeted to the recording location (Figure 4H). At 0.5 mm away, activity was also strongly suppressed, but at 2 mm, activity was similar to baseline. This distance dependence matches what has been described for clear-skull preparations at similar laser powers (Li et al., 2019). These experiments demonstrate that our SHIELD implant is fully capable of targeted optogenetics combined with Neuropixels recordings.

Distributed recordings across cortical and subcortical circuits reveal distinct visual and sensorimotor modules during alpha-like oscillations

It has long been recognized that cortical activity, even in primary sensory areas, is profoundly modulated by the brain's intrinsic dynamics (Buzsaki, 2006). The dominant such brain rhythm in awake primate cortex is alpha activity (8-12 Hz), first documented by Hans Berger in the 1920's (Berger, 1929). Since this discovery, understanding how internally generated rhythms organize the flow of activity across brain regions remains a deep question in systems neuroscience.

Recent studies in mouse visual cortex have described low-frequency (3-5 Hz) oscillations in the membrane potential of superficial neurons (Arroyo et al., 2018; Einstein et al., 2017; Nestvogel and McCormick, 2022) and in local field potential (LFP) recordings (Senzai et al., 2019). Like alpha activity, these oscillations occur during quiet wakefulness, and are abolished during periods of high arousal or locomotion (Arroyo et al., 2018; Nestvogel and McCormick, 2022). They have therefore been proposed as an evolutionary precursor to the primate alpha rhythm (Senzai et al., 2019). Yet, since these studies were focused on primary visual cortex, it is unclear how these events impact spiking brain-wide.

We leveraged our SHIELD preparation to simultaneously monitor spiking activity across many cortical and subcortical brain regions. We then asked 1) when mouse alpha events occur in VISp, do they modulate spiking activity in other areas? If so, with what specificity? And 2) are alpha events in the mouse always associated with VISp activity, or can they engage distinct sets of cortical areas independently?

To answer these questions, we performed simultaneous recordings from up to six Neuropixels probes targeted to occipital, midline, and frontal cortical regions as well as the hippocampus, thalamus, striatum, and midbrain. Consistent with previous studies, we observed prominent, rhythmic 3-5 Hz waves of activity in VISp (Figure 5A, left). These alpha events spanned all cortical layers and were characterized by brief spike bursts separated by longer silent periods lasting ~200 ms, during which the cortex was almost completely inactive. These events were not restricted to VISp, but were commonly observed to coincide with synchronous bursts and silences

across all visual cortical areas, as well as primary and secondary visual thalamus (LGd and LP), medial cortical structures (e.g. RSP), and the caudoputamen (CP).

Notably, in the same recordings, we often observed similar rhythmic spiking in primary motor cortex (MOp) (Figure 5A, right). These MOp alpha-like events occurred in a slightly higher frequency band (5-7 Hz), and often coincided with synchronous activity in primary somatosensory cortex (SSp) and somatosensory thalamus (POm). Neither visual nor motor events appeared to engage the hippocampus.

To investigate these events more systematically, we algorithmically identified alpha activity based on rhythmic population spiking in either VISp or MOp (Methods). Like primate alpha rhythms, VISp and MOp events tended to occur during periods of low arousal when the animal was immobile and had a small pupil diameter (i.e., during alpha events pupil diameter was ~25% smaller relative to randomly chosen experiment times) (Figure 5B). The VISp events were often triggered by the offset of visual stimulation (Figure 5B), as described in previous studies (Arroyo et al., 2018; Einstein et al., 2017). Activity during post-stimulus alpha events was weakly but significantly correlated with activity during the preceding stimulus, indicating that alpha events tend to replay recent sensory stimulation (Figure S4). The timing of MOp events was not related to visual stimuli (Figure 5B).

Initial inspection of example experiment rasters suggested that VISp and MOp events engaged distinct networks of cortical and subcortical regions (Figure 5A). To test this observation, we calculated cross-correlograms (CCGs) between population spiking activity in either VISp or MOp and other cortical and subcortical areas recorded during the alpha events (Figure 5C). During VISp events, VISp activity was tightly coupled to secondary visual thalamus (LP) and VISl (mouse V2), as evidenced by sharp peaks in the CCG at near-zero lag. VISp was not strongly coupled to somatosensory thalamus (PO) or primary somatosensory cortex (SSp). Indeed, coherence analysis revealed a prominent peak in the 3-7 Hz band between VISp population spiking activity and LP and VISl, but not POm or SSp (Figure 5D). Conversely, MOp showed the opposite pattern: strong coupling to PO and SSp in the 3-7 Hz band, but not to LP or VISl. Time lags between VISp and MOp and their associated regions in the 3-7 Hz band straddled zero lag, suggesting events may be initiated at multiple nodes in each network (Figure 5E).

Quantifying coherence across all simultaneously recorded regions further revealed distinct visual and sensorimotor alpha rhythm networks (Fig 5F). In addition to visual cortico-thalamic regions, visual alpha events enhanced coherence between VISp and medial cortical structures ACA and RSP, as well as the caudoputamen (CP), all of which are known to receive direct visual cortical projections (Oh et al., 2014). Conversely, MOp events enhanced coherence between MOp and SSp/POm, as well as motor-related midbrain structures MRN and deep layers of the superior colliculus (SCiw).

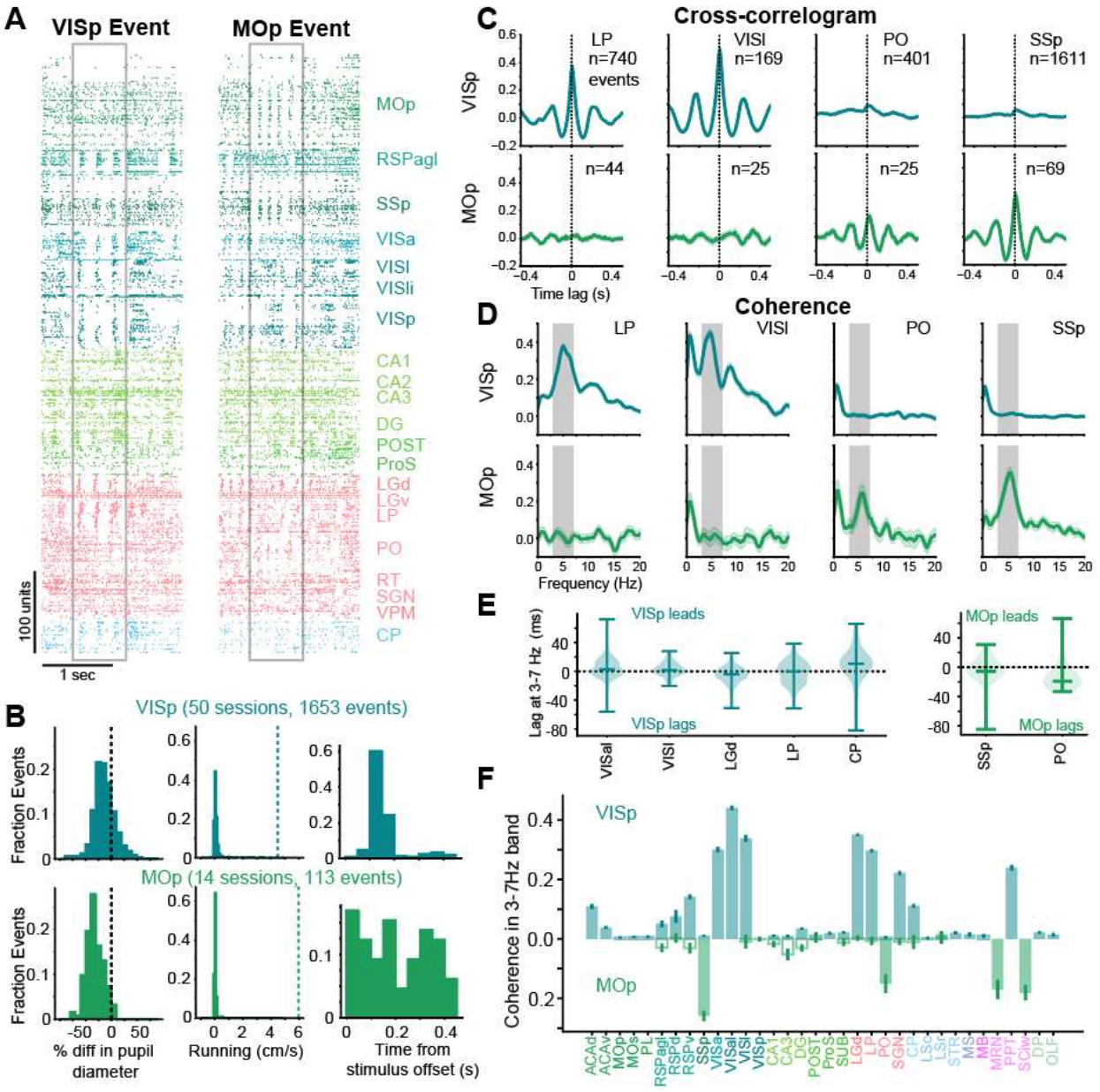

Figure 5 | Distributed coupling of visual and motor networks during alpha- and mu-like cortical oscillations. A) Population spike rasters triggered on example VISp (left) and MOp (right) oscillatory events. Both rasters are taken from the same recording session. Spikes are colored by their CCF area designation. Within a given area, units are ordered by depth. **B)** (Left) Histogram of pupil diameter during alpha event relative to random experiment times for VISp events (top, blue) and MOp events (bottom, green). (Middle) Histogram of running speed during event relative to random times (dotted line). (Right) Histogram of event onset times relative to visual stimulus offset. **C)** (Top) Cross-correlograms of population spiking activity between VISp and LP, VISl, PO, and SSp during VISp events. (Bottom) As above, but between MOp and the same four areas during MOp events. **D)** (Top) Coherence in population spiking activity between VISp and LP, VISl, PO, and SSp during VISp events relative to random experiment times. Dark rectangle indicates 3-7 Hz band. (Bottom) As above, but for MOp during MOp events. **E)** Distribution of time lags in the 3-7 Hz band across during VISp-triggered (left) and MOp-triggered (right) events. **F)** Mean coherence in population spiking activity between VISp (top, blue) and 34 CCF brain regions during

VISp events. Coherence between MOp (bottom, green) and the same 34 regions is plotted as downward going. Shaded boxes indicate significant values after correction for multiple comparisons.

Alpha-coherence reveals fine-scale functional coupling between visual cortex and striatum

We next asked whether alpha-coupling could reflect finer-scale functional connectivity between VISp and downstream targets. We chose to analyze the caudoputamen (CP) of the striatum, since it is known to receive direct projections from VISp and visual thalamus (Foster et al., 2021; Oh et al., 2014) and displays diverse sensory and motor-related responses (Peters et al., 2021; Reig and Silberberg, 2014). We hypothesized that even for a given insertion, CP units that displayed 'pure' visual responses to passively presented receptive field mapping stimuli (small gabor patches) would have stronger coherence with VISp during alpha events than CP units that did not have visual responses.

To test this, we first identified visually responsive CP units as those that were significantly modulated by the receptive field mapping stimulus (Figure 6A). This stimulus was shown outside the context of active behavior and was never associated with reward. We found that a population of CP units (CP-RF) did indeed display significant spatial receptive fields. These units were biased towards medial dorsal striatum mid-way along the anterior-posterior extent of CP (Figure 6B,C: note that we did not sample far lateral or posterior striatum).

Having split CP units into CP-RF and CP-noRF populations based on passive viewing of small gabor patches, we next compared their responses to full-field natural image presentations during active behavior. CP-RF units showed significantly larger visual responses to this stimulus compared to CP-noRF units (Figure 6D). In addition, the response time course of these two populations was different: CP-RF lagged behind VISp responses by ~20 ms, whereas CP-noRF had slower responses that lagged behind CP-RF units by an additional 20 ms. This finding thus validates our parcellation of these units with an independent visual stimulus.

Finally, we tested whether CP-RF and CP-noRF units were differentially engaged by VISp alpha oscillations. We first computed population peristimulus time histograms (PSTHs) of the activity of the two CP groups triggered on the onset of VISp alpha events (Figure 6E). We found that CP-RF firing rates were significantly more modulated, particularly during the troughs of the oscillation when the visual cortical network shuts down and direct input from visual cortex and thalamus would thus be eliminated. Next, we computed coherence between VISp and the two CP populations during VISp alpha events (Figure 6F). As predicted, CP-RF units displayed higher coherence with VISp in the 3-7 Hz band, indicating that alpha events coordinate functionally related cortico-striatal subnetworks.

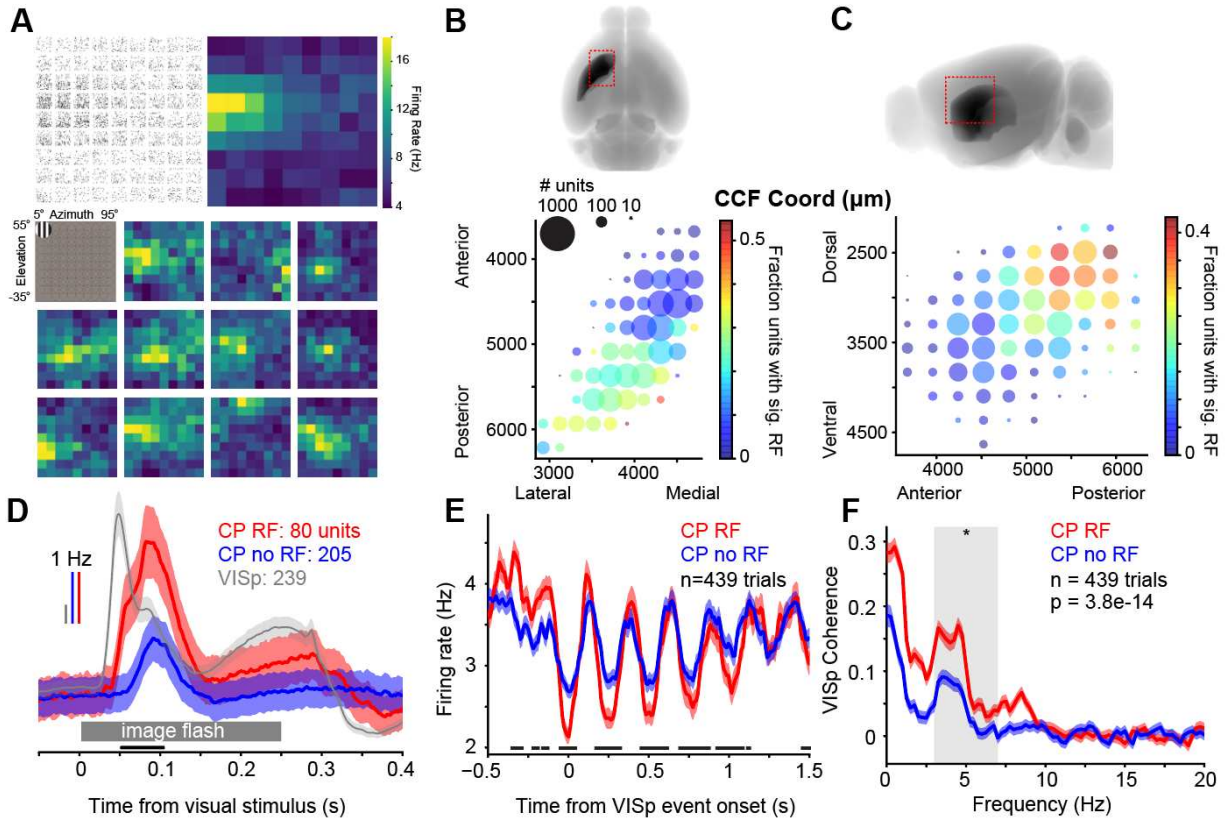

Figure 6 | Visually-responsive striatal units are more tightly coupled to VISp alpha events. A) (Top) Receptive field measured for one example unit in CP displayed as a raster (left) showing spiking activity over 30 stimulus trials and as a heatmap of the mean response (right). (Bottom) Receptive fields for 11 more example CP units together with a diagram of the receptive field-mapping stimulus (upper left). **B)** (Top) Diagram of the mouse brain in horizontal orientation showing the position of CP (dark structure) and the CCF coordinates of the plot below (red dashed rectangle). (Bottom) Bubble plot depicting the recording locations of CP units projected onto the horizontal plane. The size of each circle indicates the number of units recorded at that CCF coordinate. The color indicates the fraction of units that had significant receptive fields. **C)** Same as B, but for the sagittal orientation. **D)** Population visual response of CP units with significant RFs (red), CP units without RFs (blue), and VISp units to a full-field natural image presentation for 250 ms. **E)** Population firing rates for CP-RF and CP-noRF units triggered on VISp alpha events. Black lines at the bottom of (D,E) indicate timepoints at which activity in the two CP populations was significantly different at $p<0.05$ after correction for multiple comparisons. **F)** Coherence of population spiking between the two CP populations and VISp during VISp alpha events.

DISCUSSION

High-density silicon probes such as Neuropixels are transformative for systems neuroscience studies due to the nature and scale of the data they can collect. However, fully harnessing the power of these tools necessitates new surgical and experimental methodologies. In this study, we describe a highly flexible and robust workflow for engineering custom 3D-printed cranial implants that support user-defined multi-probe recording configurations across the mouse brain. This methodology delivers on the essential requirements for next-generation recordings in systems

neuroscience, including brain-wide targeting, simultaneous multi-area recordings, and compatibility with behavior, optogenetics, and functional imaging.

Our methodology is highly robust and has been used to make stable, high-quality recordings from 25 mice (87 experiments and 513 probe insertions). Thus, this work goes beyond mere proof-of-concept and provides a rigorously vetted set of procedures for brain-wide recordings in behaving mice. The methods we describe should be easy to implement and adopt by many labs currently performing large-scale extracellular electrophysiological recordings with Neuropixels or other silicon probe devices. The cranial implant we describe is straightforward to fabricate in-house using a commercially available and relatively low-cost 3D printer. Moreover, we provide CAD files that can serve as a starting point for users to design their own custom implants using standard CAD software such as Solidworks.

In a typical experiment for this study, we made simultaneous Neuropixels recordings from six probes that, in a single session, provided spike measurements from an average of 1,800 units across 25 brain regions. Moreover, an important aspect of the SHIELD preparation is that it supports multi-day probe insertions into different target regions. This expands the set of data that can be collected from each mouse and can reduce the number of mice needed for an experimental study. Multi-day recordings from the same mouse also provide powerful internal control data collected from a variety of brain regions (for instance, we were able to compare alpha-like rhythms from both visual and motor brain networks). Finally, multi-day recordings are important for experiments with behaving mice trained for weeks or months on complex behavioral tasks, where the value of each successfully trained mouse is considerable. In our experiments (Figures 5 and 6), we made recordings from behaving mice on four successive days. Thus, the SHIELD methodology provides high-yield, multi-area and multi-day recordings for large-scale spiking datasets in the context of active behavior.

Comparison with other methods

Virtually all previous studies making multi-Neuropixels recordings in the mouse brain have used the multiple small craniotomy approach in which holes are drilled into the mouse skull on the day of the recording (Figure 1A) (Chen et al., 2023; IBL et al., 2022; McBride et al., 2023; Steinmetz et al., 2019; Stringer et al., 2019; Vesuna et al., 2020). As described in the Introduction, this approach, while flexible, has many drawbacks. Thus, the methodology we describe here should prove extremely valuable for future studies that seek to make multi-probe recordings from distributed regions of the mouse brain.

An antecedent to the SHIELD implant we describe is the “See-Shells” methodology which was primarily developed for high-quality imaging of the dorsal surface of the mouse cortex (Ghanbari et al., 2019). See-Shells is a multi-component cranial implant assembly that includes a PET film that directly covers the dorsal cortex (after skull removal surgery). The PET film was optimized for optical clarity to support both 2-photon calcium imaging and 1-photon widefield imaging, but Ghanbari et al. also made proof-of-concept electrophysiological recordings through a single perforation in the PET film, made after the implant was installed on the brain. In the present study, we generated implants with up to 21 holes; this allows many distinct multi-probe insertion configurations, each targeting different sets of brain areas for simultaneous recording. Moreover, our procedure simplifies the experimental preparation, avoiding anesthesia and mitigating the risk of brain damage before recordings.

Future developments

The implant we describe in this study focuses on the left hemisphere of the mouse brain. Experiments involving bilateral sensory stimulation and spatially directed motor control will necessitate recordings from brain regions in both hemispheres. To support this, the same general approach we describe can be extended by modifying the cranial implant to extend over the right hemisphere. The larger implant will require surgical and headframe modifications, but multiple published studies have demonstrated the viability of such a dual hemisphere approach for use with 2-photon or widefield imaging applications (Ghanbari et al., 2019; Kauvar et al., 2020; Kim et al., 2016). Indeed, preliminary results in our lab demonstrate the feasibility of this method.

Because the implant is transparent, it can be combined with optical imaging to map the functional boundaries of cortical areas, as we demonstrate (Figure 3C), but importantly, this also provides the possibility for simultaneous multi-modal imaging, optogenetics, and distributed electrophysiology. Future studies could use 1-photon widefield calcium imaging to characterize broad activity dynamics across the dorsal surface of the cortex while using multi-Neuropixels recordings measure spiking activity in distributed cortical and subcortical regions (Peters et al., 2021).

The recordings we describe in this study involve acute insertions of multiple Neuropixels probes at the start of the recording session and removal at the end. Such acute recordings have proven extremely valuable for studying neural activity during sensory processing, decision-making, and behavior. It will also be important to measure how activity dynamics in the brain change over the course of days, weeks, and months. Previous studies have demonstrated the feasibility of chronic multi-channel electrode recordings in mice over weeks and months (Juavinett et al., 2019; Steinmetz et al., 2021; van Daal et al., 2021). The implant we describe here could be adapted in the future to support such chronic recordings.

Scientific use case: Alpha oscillatory events engage distinct cortical-subcortical networks

Alpha rhythms are the strongest electrophysiological signature of the awake brain and have been the subject of intense study since their first description by Hans Berger almost a century ago (Berger, 1929). Originally thought to reflect cortical ‘idling’ (Pfurtscheller et al., 1996) due to their prominence during quiet wakefulness, they have since been hypothesized to play an important role in regulating information transmission between cortical areas to subserve a number of cognitive processes, including working memory and attention (Saalmann et al., 2012; Von Stein and Sarnthein, 2000). Human studies have typically measured alpha activity with non-invasive electrophysiological techniques such as EEG and MEG or, in some cases, intracranial electrocorticogram arrays (Halgren et al., 2019). In non-human primates, laminar probe arrays have measured alpha rhythms across the depth of cortex in multiple sensory regions (Haegens et al., 2015). However, interpretation of these results is complicated by poor spatial resolution and volume conduction from nearby structures. Moreover, these techniques are indirect measures of neural activity and thus cannot reveal the spike output of a given region, much less the activity of individual neurons, making it impossible to determine whether alpha events engage circuits with cell-type specificity.

Together with recent advances in silicon probe technology, our preparation is ideally suited to capture coordinated activity across distributed cortical and subcortical regions with neuron resolution. We therefore set out to characterize how alpha events shape spiking activity across diverse brain areas. Building on recent studies that have described alpha-like oscillations in

mouse primary visual cortex (Arroyo et al., 2018; Einstein et al., 2017; Nestvogel and McCormick, 2022; Senzai et al., 2019), we extended these findings in several important ways.

First, we show that alpha events identified in VISp reach beyond the VISp-LGd cortico-thalamic loop, modulating spiking activity across higher visual areas but also medial cortical regions RSP and ACA, as well as the striatum. Taken together with our observation that alpha events in VISp replay recent sensory activation (Figure S4), our data support a role for alpha rhythms in facilitating plasticity across the wider visual network in the mouse brain (Han et al., 2008).

Second, we find that alpha events in the mouse are not restricted to the visual cortex. We recorded similar rhythmic patterns of spiking activity in MOp. Strikingly, MOp and VISp events engage complementary networks of cortical and subcortical brain regions, with MOp showing tight coupling to SSp and secondary sensory thalamic nucleus POm and midbrain motor structures. Like VISp alpha activity, MOp events occurred during periods of low arousal and immobility and thus resembled a motor-analog of alpha in primates, typically referred to as the mu rhythm (Arroyo et al., 1993). In rats, mu-like events (termed high-voltage spindles) have been studied in the sensorimotor system (Buzsaki et al., 1988) and found to propagate to the brainstem (Nicolelis et al., 1995). These findings suggest that alpha activity should be construed as a family of rhythms (Buzsaki, 2006), potentially generated by similar mechanisms but coordinating activity across distinct subnetworks of functionally related cortical and subcortical regions.

Finally, we leveraged the single-neuron resolution of Neuropixels recordings to investigate fine-scale functional interactions between VISp and the striatum during alpha events. We found a population of CP units with robust visual receptive fields. Though visual responses in mouse striatum have not been extensively characterized, the CP-RF cells described here resemble neurons recorded in the primate caudate (Hikosaka et al., 1989), which respond to visual stimuli unconditional on motor activity and have large, long-latency spatiotemporal receptive fields. CP-RF cells were intermixed with CP-noRF cells but were biased towards intermediate dorsomedial regions of the striatum known to receive visual projections (Bennett et al., 2019; Hintiryan et al., 2016). During VISp alpha events, CP-RF cells had greater firing rate modulation and higher coherence with VISp population activity than CP-noRF cells, suggesting fine-scale functional specificity in VISp-striatal coupling. In rats, motor-related dorsolateral striatum participates in high-voltage spindles (Berke et al., 2004), and coherence between striatal cells and MOp was found to increase over the course of learning a brain-machine interface (BMI) task (Koralek et al., 2013). In that task, cortico-striatal coherence was specific to the population of MOp neurons used to control the BMI. Together with our findings, these results suggest that highly specific coupling during alpha activity is a hallmark of cortico-striatal interactions. Such specificity may play an important role in plasticity and learning.

Conclusion

To understand the intricate neuronal processes underlying complex behavior and cognition, it is imperative to simultaneously measure fast timescale spiking activity across numerous interacting brain regions. While advancements like Neuropixels have enabled increasingly large numbers of neurons to be recorded, substantial methodological and surgical challenges remain to fully capitalize on their potential, particularly for concurrent multi-probe recordings. Our innovative SHIELD methodology provides an elegant solution for accessing and recording from the mouse brain with many simultaneously inserted Neuropixels probes, allowing dozens of regions and

thousands of neurons to be measured in a single mouse. This timely addition to the field enables cutting-edge experiments that will uncover new insights into the mechanisms of distributed computation and multi-regional signal flow dynamics across the brain.

ACKNOWLEDGEMENTS

We thank the Allen Institute founder, Paul G. Allen, for his vision, encouragement and support. funding for this project was provided by the Allen Institute. We thank the Transgenic Colony Management and Laboratory Animal Services teams for caring for the mice in this study. We thank the Imaging team for performing Tissuecyte imaging. We thank Suhasa Kodandaramaiah and members of his laboratory for discussion and advice regarding methods associated with their "See-Shells" methodology.

AUTHOR CONTRIBUTIONS

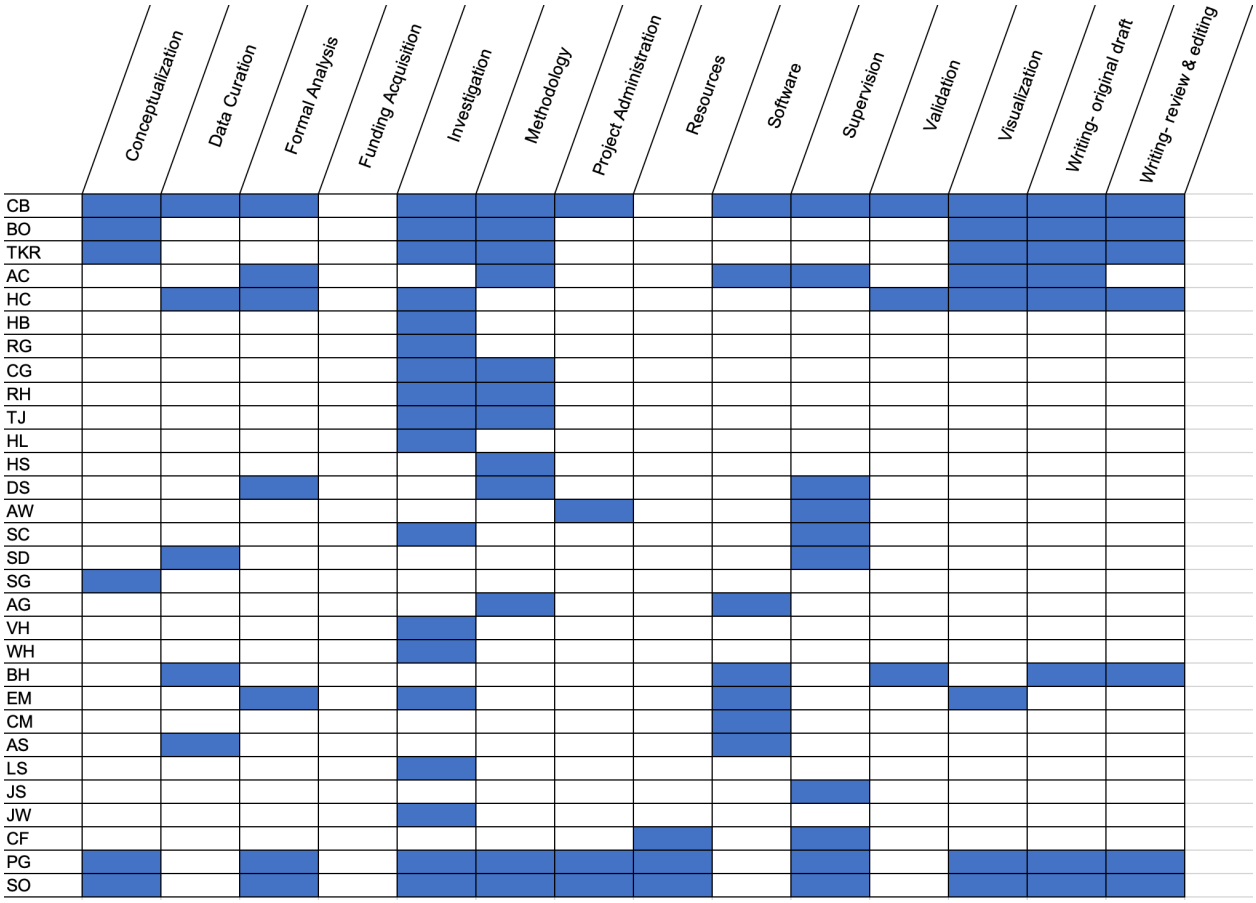

EXPERIMENTAL MODEL AND SUBJECT DETAILS

Mice

Mice were maintained in the Allen Institute animal facility and used in accordance with protocols approved by the Allen Institute's Institutional Animal Care and Use Committee. Electrophysiology experiments used C57BL/6J wild-type mice purchased from Jackson Laboratories at age P25-50 (n = 7) and three transgenic lines (n = 1 VGAT-ChR2, n = 14 Sst-IRES-Cre; Ai32, and n = 4 Vip-IRES-Cre; Ai32, 18 males and 8 females). For skull contour mapping, eight mice were used (n= 3 Vip-IRES-Cre;Ai148, n=4 Slc17a7-IRES2-Cre;Camk2a-tTA;Ai93, n=1 Sst-IRES-Cre;Ai148, 5

males and 3 females). Following surgery, all mice were single-housed and maintained on a reverse 12-hour light cycle in a shared facility with room temperatures between 68º and 72ºF and humidity between 30 and 70%. All experiments were performed during the dark cycle. During behavior training, mice were water restricted to 85% of their initial body weight, with ad libitum access to food.

METHOD DETAILS

Headframe

To enable co-registration across surgical, intrinsic signal imaging, and electrophysiology rigs, each animal was implanted with a 3D-printed, grade 5 titanium headframe (Groblewski et al., 2020b). In addition to a standard clamping interface, the headframe includes a modified L-shaped portion that contacts the right hemisphere parietal skull plate. The headframe is affixed with a black acrylic photopolymer well with an exposed gold pin for grounding recordings.

Implant design

The implant dimensions are defined in CAD. Total thickness of the implant is nominally 650µm, with the 'stump' portion (i.e., the part that is inserted into the craniotomy) 400µm thick, and the 'flange' 250µm thick. The flange is larger than the craniotomy by 600µm and sits on top of the mouse skull, which provides an area to apply glue and to set the implant orientation in 3D space.

To design the implant in CAD software, we started with a triaxial ellipsoid-like surface matching the curvature of an average mouse skull. This design was defined by three curves positioned with respect to Bregma (Figure S1). The ellipsoid-like surface is then generated using the Solidworks 'Surface Fill' function with the patch boundary being the ellipse, and the constraint curves being the circular section curves. The next step is to cut the ellipsoid-like surface, once for the shape of the craniotomy, and again for the shape of the flange, resulting in two surfaces. The final shapes for these surfaces were created using an iterative feedback process, during which surgeons tested prototypes and provided feedback referenced to stereotaxic measurements. Once the craniotomy and flange surfaces have been cut, holes are sketched on the Bregma-Lambda plane and dimensioned with respect to Bregma. A typical hole size is 750 µm. No holes should be in the flange portion of the implant, and holes should not overlap. Holes are cut into both the stump and flange surfaces using the 'surface-trim' feature in Solidworks. 'Thicken' operations are performed on the two surfaces. The larger flange surface is thickened up 250 µm. The smaller stump surface is thickened down 400 µm. The final step of the design process is to add 45-degree chamfers to the tops of the insertion holes. The chamfers allow flexibility in probe angles and also make it easier to fill the holes with SORTA-Clear.

Implant CAD files are exported as .stl files and imported into Formlabs PreForm for printing on a Formlabs Form 3+ printer in clear resin at 25 µm layer height. After printing, the implants are washed in a dedicated isopropyl alcohol bath (Formlabs Wash Station) maintained at 99% concentration for 10 minutes. The implants are then UV cured in the Formlabs Cure station at 60ºC for 15 minutes. Prior to implanting, the implant is coated with SORTA-Clear 18™ silicone rubber (Smooth-On; Figure 2A). SORTA-Clear improves optical clarity for brain health evaluations and optical imaing and protects the brain until electrophysiology. SORTA-Clear is mixed and

degassed following manufacturer recommendations. Implants are pressed into a putty mold (ComposiMold, ImPRESSive putty) to seal the underside from leaks while the SORTA-Clear cures (Figure S1). The SORTA-Clear is drawn into a 1mL syringe, then a blunt 25G needle is attached for dispensing into the holes. Each hole must be filled individually and slowly to prevent trapping air. After each hole is filled, a thin layer is applied over the dorsal surface of the implant overlying the craniotomy, and the molds are left to cure for 24 hours. Coated implants are then cleaned by rinsing in 70% ethanol, placed into individual autoclave bags, and autoclaved for 5 minutes (131°C, 14.7 psi).

Surgical procedure for hemispheric craniotomy

A pre-operative injection of dexamethasone (3.2 mg/kg, S.C.) is administered 1 h before surgery to reduce swelling and postoperative pain. Mice are initially anesthetized with 5% isoflurane (1-3 min) and placed in a stereotaxic frame (Model# 1900, Kopf). Isoflurane levels are maintained at 1.0-2.0% and body temperature is maintained at 37.5°C for the duration of the surgery. Carprofen is administered for pain management (5-10 mg/kg, S.C.), and atropine is administered to suppress bronchial secretions and regulate heart rhythms (0.02-0.05 mg/kg, S.C.). An incision is made on the dorsal surface of the skull, and skin is removed in a teardrop shape, exposing the rostral rhinal vein between the eyes, the dorsal surface of the parietal and occipital skull plates, and stopping where the neck muscle begins to attach to the back of the skull. Next, the periosteum is removed from the skull surface to improve adhesion of the cement to the skull and prevent future scabbing and infection. Starting posterior of the left eye, angled forceps are used to separate cheek muscle from the skull, as well as connective tissue and muscle above the left ear. The cheek muscle is then pulled away from the skull and is stretched out so that it makes a seal with the left lateral portion of the well. The exposed skin (and any exposed soft tissue such as the cheek muscle) is then sealed with Vetbond, and the exposed skull is leveled with respect to pitch, roll, and yaw. Once the skull is level, bregma is identified using the custom bregma stylus (Figure 2C). Without moving the stereotaxic arm in X or Y, the stylus is replaced with a custom “tracer” (Figure 2C) that provides a guide for marking the craniotomy with respect to bregma. A #11 scalpel blade (or forceps) is used to etch a faint line in the skull around the tracer, which is then replaced with a shallow trench by lightly drilling, without breaking through the skull (NeoBurr EF4). After etching is complete, the tracer is replaced with the headframe, which is then lowered in Z to make contact with the skull. Next, dental cement (C&B Metabond, Parkell) is used to attach the headframe to the skull. Once the cement has hardened, the headframe is clamped into a custom frame and the craniotomy and durotomy are performed. The autoclaved custom implant is then attached to the skull by applying light-curable glue (Loctite 4305) between the flange and skull which is then hardened with blue light. Any areas of exposed skull are then covered with cement. Any white cement on the inside of the well is coated with a layer of black cement to reduce glare during ISI imaging. The mouse is given 1.0-1.5mL Lactated Ringers Solution (LRS) to help recover from the surgery and replace lost fluids. After removing the mouse from anesthesia, but prior to it waking up, a spatially registered image of the cranial window is obtained using a custom imaging system. Finally, a removable plastic cap is placed over the well to protect the coated implant from cage debris, and the mouse is returned to its home cage for recovery. Over the following 7-14 days, mice are monitored regularly for overall health, cranial window clarity, and brain health.

Intrinsic Signal Imaging

Intrinsic signal imaging (ISI) was used to delineate functionally defined visual area boundaries (Garrett et al., 2014; Juavinett et al., 2017) to enable targeting of Neuropixels probes to retinotopically defined locations in primary and secondary visual areas as described previously (Siegle et al., 2021). Briefly, mice were lightly anesthetized (1-1.4% isoflurane) and eye drops (Lacri99 Lube Lubricant Eye Ointment; Refresh) were applied. Next a vasculature image was obtained under green light, then the hemodynamic response to a visual stimulus was imaged under red light. The stimulus consisted of an alternating checkerboard pattern (20º wide bar, 25º square size) moving across a mean luminance gray background. On each trial, the stimulus bar was swept across the four cardinal axes 10 times in each direction at a rate of 0.1 Hz. Up to 10 trials were performed on each mouse. A minimum of three trials were averaged to produce altitude and azimuth phase maps, calculated from the discrete Fourier transform of each pixel. A "sign map" was produced from the phase maps by taking the sine of the angle between the altitude and azimuth map gradients. In the sign maps, each cortical visual area appears as a contiguous red or blue region (Figure 3C).

Skull contour mapping

Mice were prepared for surgery and anesthetized as described above. A headplate was installed, and the scalp was removed to reveal the skull. The mouse was then euthanized and scans were acquired ex vivo with a Micro Epsilon Laser Line Scanner. The point clouds from each scan were converted to a surface using Geomagic Design X. All skull surfaces were then imported into Solidworks.

Implant preparation prior to Neuropixels recordings

SORTA-Clear plug removal and agarose application

To prepare the brain for recording, the SORTA-Clear coating over the implant is removed and replaced with a temporary layer of Kwik-Cast (World Precision Instruments). The mouse is anesthetized with isoflurane (5% induction, 1-2% maintenance, 100% O2) and eyes protected with ocular lubricant (IDrop, VetPLUS). Body temperature is maintained at 37.5°C (TC-1000 temperature controller, CWE, Incorporated). The well is cleaned of any debris using ethanol swabs. Then, the inside of the well surrounding the SORTA-Clear plug is painted with white Metabond to improve visibility during probe insertion. Once the Metabond is dry, the well is flooded with enough ACSF to completely submerge the SORTA-Clear sheet, which is then removed with small forceps, starting at the anterior or posterior end of the sheet and peeling gently to remove it in one piece. Once the SORTA-Clear sheet is completely detached from the implant, the edges of implant holes are tested with small forceps to ensure all holes are free of SORTA-clear or debris. ACSF is removed from the well using Sugi spears (Kettenbach) and the well is filled with Kwik-Cast. Once the Kwik-Cast is fully dry, a plastic protective cap is secured on the well to protect against debris and the mice are returned to their home cage. This preparation is stable for at least three days before the recording.

Neuropixels recordings

Preparation of mouse for recording

The mouse is removed from its home cage and clamped to the running wheel on the experimental rig. Wheel height is adjusted as needed for each mouse. Once head-fixed, the protective well cap and Kwik-Cast layer are removed. The ground wire is tucked into the side of the well and any excess debris cleaned using a Sugi spear or cotton tipped applicator. Approximately 0.4 ml of agarose is applied in a smooth layer over the entire implant surface and ground wire. After popping any large bubbles, the agarose is allowed to set for ~10 seconds. To prevent the agarose from drying out during the experiment, a layer of silicon oil is applied over exposed agarose with a toothpick.

Application of CM-DiI and DiO to probes

In our experiments, probes were inserted into the same mouse on sequential days. To distinguish the paths of these different penetrations, we used two dyes, CM-DiI (1 mM in ethanol; ThermoFisher Product #V22888) and DiO (1mM in ethanol; ThermoFisher Product #V22886), on separate recording days. The probes were coated with dye before recordings by immersing them at least 3mm into a well filled with dye. Each probe was dipped five times to ensure adequate coating.

Probe insertion

Our custom experimental rig can insert up to six Neuropixels probes simultaneously (Durand et al., 2022). Each probe is mounted on a separate 3-axis micromanipulator with a 15 mm travel range (New Scale Technologies, Victor, NY). Probe and implant hole combinations were selected prior to each experiment. Probes were driven to target their selected holes and lowered to the surface of the brain while the operator watched real-time signals on the OpenEphys GUI to identify activity indicative of the brain surface. If the probe needed adjustment when attempting to insert (e.g. to avoid vessels), the probe was completely retracted out of the silicon oil to prevent probe bending. If a probe could not be inserted into its assigned hole, another target hole was selected. Once all probes reached the brain surface, each probe was zeroed and set to insert 3000 μm at 200 μm/min. Insertion of a probe was stopped if it bumped other probes (when probes target nearby locations, care must be taken to avoid collisions between the probe bases). Once all probes reached their final depth, the probes were allowed to settle for 10 minutes, and photo documentation of the inserted probes was captured. In a subset (23) of recordings, probes were inserted to 3100 μm then retracted 100 μm to their final depths to reduce tissue compression and subsequent electrode drift relative to the brain (Figure S3).

Our goal was to insert 6 probes per session. Overall, we achieved a penetration success of 5.46 probes per session, with failures due to dura regrowth, collisions with other probes, or probe breakage during manipulation. To facilitate insertion through dura regrowth, the tips of two of six Neuropixels probes were sharpened as previously described (Durand et al., 2022), which we found to effectively reduce insertion failures (Figure S3).

Probes and grounding

All neural recordings were carried out with Neuropixels 1.0 probes, as previously described (Durand et al., 2022; Siegle et al., 2021). The 383 electrodes closest to the tip were used, providing a maximum of 3.84 mm of tissue coverage. The signals from each recording site are

split in hardware into a spike band (30 kHz sampling rate, 500 Hz highpass filter) and an LFP band (2.5 kHz sampling rate, 1000 Hz lowpass filter).

A 32 AWG silver wire (A-M Systems) is epoxied to the headframe during the implant surgery and serves as the ground connection. The wire is pre-soldered to a gold pin embedded in the headframe well, which mates with a second gold pin on the protective cone. This second gold pin is connected to both the behavior stage and the probe ground. Prior to the experiment, the brain-to-probe ground path was checked using a multimeter. The reference connection on the Neuropixels probes was permanently soldered to ground using a silver wire, and all recordings were made using the tip reference configuration. The headstage grounds (which are contiguous with the Neuropixels probe grounds) were connected with 36 AWG copper wire (Phoenix Wire). All probes were connected in parallel to animal ground.

Data acquisition

Neuropixels data was acquired at 30 kHz (spike band) and 2.5 kHz (LFP band) using the Open Ephys GUI (Siegle et al., 2017). Gain settings of 500x and 250x were used for the spike band and LFP band, respectively.

Videos of the eye, body, and face were acquired at 60 Hz. The angular velocity of the running wheel was recorded at the time of each stimulus frame, at approximately 60 Hz. Synchronization signals for each frame were acquired by a dedicated computer with a National Instruments card acquiring digital inputs at 100 kHz, which was considered the master clock. A 32-bit digital "barcode" was sent with an Arduino Uno (SparkFun DEV-11021) every 30 s to synchronize all devices with the neural data.

To synchronize the visual stimulus to the master clock, a silicon photodiode (PDA36A, Thorlabs) was placed on the stimulus monitor above a "sync square" that flipped from black to white every 60 frames.

Probe removal and cleaning

At the end of the recording sessions probes were removed slowly from the brain (approximately 1 mm/minute). A Sugi spear was used to clear off excess silicone oil from the implant and forceps were used to remove the agarose. The well was filled with Kwik-Cast, allowed to dry for ~30 seconds, and then the well cap was replaced.

To remove debris, probes were submerged in a 1% Tergazyme solution overnight then rinsed in deionized water the next day.

Visual stimulation and behavior

Mice were trained to perform a visual change detection task in which one of 8 natural images was continuously flashed (250 ms image presentation followed by 500 ms gray screen) and mice were rewarded for licking when the image identity changed. The change detection task is described in previous publications (Garrett et al., 2020; Groblewski et al., 2020a).

Receptive fields were mapped during each experiment using Gabor stimuli windowed to have a 20 degree diameter and presented in a 9x9 grid. Grid positions were spaced by 10 degrees. Gabors had a temporal frequency of 4 Hz, a spatial frequency of 0.08 cycles/degree and were shown at 3 orientations (0, 45, 90 degrees). They were 250 ms in duration without gaps between stimuli. There were 15 trials for each condition (81 positions, 3 orientations).

Ex vivo imaging and analysis to identify probe tracts

Tissuecyte imaging

Serial two-photon tomography was used to obtain a three-dimensional (3D) image volume of coronal brain images for each specimen. This 3D volume enables spatial registration of each mouse's brain to the Allen Mouse Common Coordinate Framework (CCF). Methods for this procedure have been described in detail in whitepapers associated with the Allen Mouse Brain Connectivity Atlas and in Oh et al (Oh et al., 2014).

Probe track annotation and CCF Registration

Probe tracks were annotated manually in the Tissuecyte image volume after resampling to 10x10x10 μm voxels. Because linear probe trajectories become curved after warping to the CCF, annotations were performed before applying local deformation to the volume, enabling us to fit a line to the annotated track points for each probe. Electrode positions were adjusted along this line based on electrophysiological features and unit density. After this refinement process, electrode coordinates were passed through the final deformation field and thus warped into the CCF.

For probe insertions into visual cortical areas, vasculature landmarks were used to warp probe insertion images to corresponding ISI images which delineated the visual area boundaries for each animal. Probe insertions were then annotated on these warped images and manually assigned to visual cortical areas based on ISI-derived visual sign maps. These manual area assignments superseded CCF area labels for cortical units.

Data pre-processing and spike sorting

Prior to spike sorting, the spike-band data passed through 4 steps: offset removal, median subtraction, filtering, and whitening. First, the median value of each channel was subtracted to center the signals around zero. Next, the median across channels was subtracted to remove common-mode noise. To remove noise sources that are shared across channels, the median was calculated across channels that are sampled simultaneously as previously described (Siegle et al., 2021). The median-subtracted data was sent to Kilosort2, which applies a 150 Hz high-pass filter, followed by whitening in blocks of 32 channels. The filtered, whitened data was saved to a separate file for the spike sorting step.

Kilosort2 was used to identify spike times and assign spikes to individual units (Pachitariu et al., 2023). The Kilosort2 algorithm will occasionally fit a template to the residual left behind after another template has been subtracted from the original data, resulting in double-counted spikes. This can create the appearance of an artificially high number of inter-spike interval violations for one unit or artificially high zero-time-lag synchrony between nearby units. To eliminate the possibility that this artificial synchrony would contaminate data analysis, the outputs of Kilosort2 was post-processed to remove spikes with peak times within 5 samples (0.16 ms) and peak waveforms within 5 channels (~50 μm).

Data analysis

Quality metric criteria for unit inclusion

Units were included for analysis if they met the following criteria: inter-spike violation rate less than 0.5, amplitude cutoff less than 0.1, and presence ratio greater than 0.95. Each of these metrics was calculated as described previously (Siegle et al., 2021).

Identification of alpha events

Alpha events in VISp and MOp were identified with the following algorithm, which was empirically found to agree with manual annotation. First, unit activity within each area was binned into 10 ms bins and averaged together to create a population spike rate, which was then smoothed with a symmetrical exponential filter (10 ms tau). Sessions with less than 20 neurons in the relevant area (VISp or MOp) were excluded in this analysis. Rhythmic pauses in activity in the resulting population trace were then identified by finding local maxima in the inverted trace (scipy.signal.find_peaks; prominence=5, height=-1, width=[100 ms, 300 ms]). An alpha event was registered if there were at least four maxima at intervals between 125 and 350 ms in a 1.25 second window. After an alpha event, we imposed a refractory period of two seconds before another event could be registered. Because this algorithm occasionally identified non-rhythmic activity, we further filtered the resulting events by requiring that the power of the autocorrelogram in the 3-7 Hz band exceed 0.1 $(\text{spikes/sec})^2$.

Cross-correlograms and coherence

For each session, cross-correlograms (CCGs) were computed between the population activity of VISp or MOp and all other regions for which at least 20 neurons were recorded. CCGs were computed for 2 second windows centered on the alpha event and were normalized so that the auto-correlogram had a peak of 1. CCGs for each area pair were then pooled across sessions for subsequent analysis.

Multi-taper coherence was computed using the nipy software package (https://github.com/nipy/nitime) for four second windows centered on each alpha event. To isolate coherence due to alpha rhythms, coherence was also calculated for random times during each session and subtracted from coherence calculated during alpha events.

Receptive Field Mapping

The receptive field for one unit was defined as the 2D histogram of spike counts at each of 81 locations of the Gabor stimulus (9 x 9 matrix). The significance of a given unit's receptive field was measured with a chi-square test, as described previously (Siegle et al., 2021). Any unit with a p-value less than 0.01 was considered to have a significant receptive field.

Statistics

Unless otherwise specified, paired comparisons were made with the Wilcoxon signed-rank test and unpaired comparisons with the Wilcoxon rank-sums test. For panels with multiple comparisons, p-values were corrected with the Benjamini-Hochberg method.

REFERENCES

Allen, W.E., Chen, M.Z., Pichamoorthy, N., Tien, R.H., Pachitariu, M., Luo, L., Deisseroth, K., 2019. Thirst regulates motivated behavior through modulation of brainwide neural population dynamics. Science 364, eaav3932. https://doi.org/10.1126/science.aav3932

Allen, W.E., Kauvar, I.V., Chen, M.Z., Richman, E.B., Yang, S.J., Chan, K., Gradinaru, V., Deverman, B.E., Luo, L., Deisseroth, K., 2017. Global Representations of Goal-Directed Behavior in Distinct Cell Types of Mouse Neocortex. Neuron 94, 891-907.e6. https://doi.org/10.1016/j.neuron.2017.04.017

Arroyo, S., Bennett, C., Hestrin, S., 2018. Correlation of Synaptic Inputs in the Visual Cortex of Awake, Behaving Mice. Neuron 99, 1289-1301.e2. https://doi.org/10.1016/j.neuron.2018.08.008

Arroyo, S., Lesser, R.P., Gordon, B., Uematsu, S., Jackson, D., Webber, R., 1993. Functional significance of the mu rhythm of human cortex: an electrophysiologic study with subdural electrodes. Electroencephalography and Clinical Neurophysiology 87, 76–87. https://doi.org/10.1016/0013-4694(93)90114-B

Bekhbat, M., Merrill, L., Kelly, S.D., Lee, V.K., Neigh, G.N., 2016. Brief anesthesia by isoflurane alters plasma corticosterone levels distinctly in male and female rats: implications for tissue collection methods. Behav Brain Res 305, 122–125. https://doi.org/10.1016/j.bbr.2016.03.003

Bennett, C., Gale, S.D., Garrett, M.E., Newton, M.L., Callaway, E.M., Murphy, G.J., Olsen, S.R., 2019. Higher-Order Thalamic Circuits Channel Parallel Streams of Visual Information in Mice. Neuron 102, 477-492.e5. https://doi.org/10.1016/j.neuron.2019.02.010

Berger, H., 1929. Über das elektroenkephalogramm des menschen. Archiv für psychiatrie und nervenkrankheiten 87, 527–570.

Berke, J.D., Okatan, M., Skurski, J., Eichenbaum, H.B., 2004. Oscillatory Entrainment of Striatal Neurons in Freely Moving Rats. Neuron 43, 883–896. https://doi.org/10.1016/j.neuron.2004.08.035

Buzsaki, G., 2006. Rhythms of the Brain. Oxford university press.

Buzsaki, G., Bickford, R.G., Ponomareff, G., Thal, L.J., Mandel, R., Gage, F.H., 1988. Nucleus basalis and thalamic control of neocortical activity in the freely moving rat. J. Neurosci. 8, 4007–4026. https://doi.org/10.1523/JNEUROSCI.08-11-04007.1988

Cardin, J.A., Crair, M.C., Higley, M.J., 2020. Mesoscopic Imaging: Shining a Wide Light on Large-Scale Neural Dynamics. Neuron 108, 33–43. https://doi.org/10.1016/j.neuron.2020.09.031

Chen, S., Liu, Y., Wang, Z., Colonell, J., Liu, L.D., Hou, H., Tien, N.-W., Wang, T., Harris, T., Druckmann, S., Li, N., Svoboda, K., 2023. Brain-wide neural activity underlying memory-guided movement. https://doi.org/10.1101/2023.03.01.530520

de Vries, S.E.J., Lecoq, J.A., Buice, M.A., Groblewski, P.A., Ocker, G.K., Oliver, M., Feng, D., Cain, N., Ledochowitsch, P., Millman, D., Roll, K., Garrett, M., Keenan, T., Kuan, L., Mihalas, S., Olsen, S., Thompson, C., Wakeman, W., Waters, J., Williams, D., Barber, C., Berbesque, N., Blanchard, B., Bowles, N., Caldejon, S.D., Casal, L., Cho, A., Cross, S., Dang, C., Dolbeare, T., Edwards, M., Galbraith, J., Gaudreault, N., Gilbert, T.L., Griffin, F., Hargrave, P., Howard, R., Huang, L., Jewell, S., Keller, N., Knoblich, U., Larkin, J.D., Larsen, R., Lau, C., Lee, E., Lee, F., Leon, A., Li, L., Long, F., Luviano, J., Mace, K., Nguyen, T., Perkins, J., Robertson, M., Seid, S., Shea-Brown, E., Shi, J., Sjoquist, N., Slaughterbeck, C., Sullivan, D., Valenza, R., White, C., Williford, A., Witten, D.M., Zhuang, J., Zeng, H., Farrell, C., Ng, L., Bernard, A., Phillips, J.W., Reid, R.C., Koch, C., 2020. A large-scale standardized physiological survey reveals functional organization of the mouse visual cortex. Nat Neurosci 23, 138–151. https://doi.org/10.1038/s41593-019-0550-9

Durand, S., Heller, G.R., Ramirez, T.K., Luviano, J.A., Williford, A., Sullivan, D.T., Cahoon, A.J., Farrell, C., Groblewski, P.A., Bennett, C., Siegle, J.H., Olsen, S.R., 2022. Acute head-fixed recordings in

awake mice with multiple Neuropixels probes. Nat Protoc 1–34. https://doi.org/10.1038/s41596-022-00768-6

Einstein, M.C., Polack, P.-O., Tran, D.T., Golshani, P., 2017. Visually Evoked 3–5 Hz Membrane Potential Oscillations Reduce the Responsiveness of Visual Cortex Neurons in Awake Behaving Mice. J. Neurosci. 37, 5084–5098. https://doi.org/10.1523/JNEUROSCI.3868-16.2017

Eng, L.F., Ghirnikar, R.S., 1994. GFAP and Astrogliosis. Brain Pathology 4, 229–237. https://doi.org/10.1111/j.1750-3639.1994.tb00838.x

Foster, N.N., Barry, J., Korobkova, L., Garcia, L., Gao, L., Becerra, M., Sherafat, Y., Peng, B., Li, X., Choi, J.-H., Gou, L., Zingg, B., Azam, S., Lo, D., Khanjani, N., Zhang, B., Stanis, J., Bowman, I., Cotter, K., Cao, C., Yamashita, S., Tugangui, A., Li, A., Jiang, T., Jia, X., Feng, Z., Aquino, S., Mun, H.-S., Zhu, M., Santarelli, A., Benavidez, N.L., Song, M., Dan, G., Fayzullina, M., Ustrell, S., Boesen, T., Johnson, D.L., Xu, H., Bienkowski, M.S., Yang, X.W., Gong, H., Levine, M.S., Wickersham, I., Luo, Q., Hahn, J.D., Lim, B.K., Zhang, L.I., Cepeda, C., Hintiryan, H., Dong, H.-W., 2021. The mouse cortico–basal ganglia–thalamic network. Nature 598, 188–194. https://doi.org/10.1038/s41586-021-03993-3

Garrett, M., Groblewski, P., Piet, A., Ollerenshaw, D., Najafi, F., Yavorska, I., Amster, A., Bennett, C., Buice, M., Caldejon, S., Casal, L., D'Orazi, F., Daniel, S., Vries, S.E. de, Kapner, D., Kiggins, J., Lecoq, J., Ledochowitsch, P., Manavi, S., Mei, N., Morrison, C.B., Naylor, S., Orlova, N., Perkins, J., Ponvert, N., Roll, C., Seid, S., Williams, D., Williford, A., Ahmed, R., Amine, D., Billeh, Y., Bowman, C., Cain, N., Cho, A., Dawe, T., Departee, M., Desoto, M., Feng, D., Gale, S., Gelfand, E., Gradis, N., Grasso, C., Hancock, N., Hu, B., Hytnen, R., Jia, X., Johnson, T., Kato, I., Kivikas, S., Kuan, L., L'Heureux, Q., Lambert, S., Leon, A., Liang, E., Long, F., Mace, K., Abril, I.M. de, Mochizuki, C., Nayan, C., North, K., Ng, L., Ocker, G.K., Oliver, M., Rhoads, P., Ronellenfitch, K., Schelonka, K., Sevigny, J., Sullivan, D., Sutton, B., Swapp, J., Nguyen, T.K., Waughman, X., Wilkes, J., Wang, M., Farrell, C., Wakeman, W., Zeng, H., Phillips, J., Mihalas, S., Arkhipov, A., Koch, C., Olsen, S.R., 2023. Stimulus novelty uncovers coding diversity in visual cortical circuits. https://doi.org/10.1101/2023.02.14.528085

Garrett, M., Manavi, S., Roll, K., Ollerenshaw, D.R., Groblewski, P.A., Ponvert, N.D., Kiggins, J.T., Casal, L., Mace, K., Williford, A., Leon, A., Jia, X., Ledochowitsch, P., Buice, M.A., Wakeman, W., Mihalas, S., Olsen, S.R., 2020. Experience shapes activity dynamics and stimulus coding of VIP inhibitory cells. eLife 9, e50340. https://doi.org/10.7554/eLife.50340

Garrett, M.E., Nauhaus, I., Marshel, J.H., Callaway, E.M., 2014. Topography and Areal Organization of Mouse Visual Cortex. J. Neurosci. 34, 12587–12600. https://doi.org/10.1523/JNEUROSCI.1124-14.2014

Ghanbari, L., Carter, R.E., Rynes, M.L., Dominguez, J., Chen, G., Naik, A., Hu, J., Sagar, M.A.K., Haltom, L., Mossazghi, N., Gray, M.M., West, S.L., Eliceiri, K.W., Ebner, T.J., Kodandaramaiah, S.B., 2019. Cortex-wide neural interfacing via transparent polymer skulls. Nat Commun 10, 1500. https://doi.org/10.1038/s41467-019-09488-0

Groblewski, Ollerenshaw, D.R., Kiggins, J.T., Garrett, M.E., Mochizuki, C., Casal, L., Cross, S., Mace, K., Swapp, J., Manavi, S., Williams, D., Mihalas, S., Olsen, S.R., 2020a. Characterization of Learning, Motivation, and Visual Perception in Five Transgenic Mouse Lines Expressing GCaMP in Distinct Cell Populations. Frontiers in Behavioral Neuroscience 14.

Groblewski, Sullivan, D., Lecoq, J., de Vries, S.E.J., Caldejon, S., L'Heureux, Q., Keenan, T., Roll, K., Slaughterback, C., Williford, A., Farrell, C., 2020b. A standardized head-fixation system for performing large-scale, in vivo physiological recordings in mice. Journal of Neuroscience Methods 346, 108922. https://doi.org/10.1016/j.jneumeth.2020.108922

Guo, Z.V., Li, N., Huber, D., Ophir, E., Gutnisky, D., Ting, J.T., Feng, G., Svoboda, K., 2014. Flow of Cortical Activity Underlying a Tactile Decision in Mice. Neuron 81, 179–194. https://doi.org/10.1016/j.neuron.2013.10.020

Haegens, S., Barczak, A., Musacchia, G., Lipton, M.L., Mehta, A.D., Lakatos, P., Schroeder, C.E., 2015. Laminar Profile and Physiology of the α Rhythm in Primary Visual, Auditory, and Somatosensory Regions of Neocortex. J. Neurosci. 35, 14341–14352. https://doi.org/10.1523/JNEUROSCI.0600-15.2015

Halgren, M., Ulbert, I., Bastuji, H., Fabó, D., Erőss, L., Rey, M., Devinsky, O., Doyle, W.K., Mak-McCully, R., Halgren, E., Wittner, L., Chauvel, P., Heit, G., Eskandar, E., Mandell, A., Cash, S.S., 2019. The generation and propagation of the human alpha rhythm. Proceedings of the National Academy of Sciences 116, 23772–23782. https://doi.org/10.1073/pnas.1913092116

Han, F., Caporale, N., Dan, Y., 2008. Reverberation of Recent Visual Experience in Spontaneous Cortical Waves. Neuron 60, 321–327. https://doi.org/10.1016/j.neuron.2008.08.026

Hikosaka, O., Sakamoto, M., Usui, S., 1989. Functional properties of monkey caudate neurons. II. Visual and auditory responses. Journal of Neurophysiology 61, 799–813. https://doi.org/10.1152/jn.1989.61.4.799

Hintiryan, H., Foster, N.N., Bowman, I., Bay, M., Song, M.Y., Gou, L., Yamashita, S., Bienkowski, M.S., Zingg, B., Zhu, M., Yang, X.W., Shih, J.C., Toga, A.W., Dong, H.-W., 2016. The mouse cortico-striatal projectome. Nat Neurosci 19, 1100–1114. https://doi.org/10.1038/nn.4332

Holtmaat, A., Bonhoeffer, T., Chow, D.K., Chuckowree, J., De Paola, V., Hofer, S.B., Hübener, M., Keck, T., Knott, G., Lee, W.-C.A., Mostany, R., Mrsic-Flogel, T.D., Nedivi, E., Portera-Cailliau, C., Svoboda, K., Trachtenberg, J.T., Wilbrecht, L., 2009. Long-term, high-resolution imaging in the mouse neocortex through a chronic cranial window. Nat Protoc 4, 1128–1144. https://doi.org/10.1038/nprot.2009.89

IBL, Banga, K., Benson, J., Bonacchi, N., Bruijns, S.A., Campbell, R., Chapuis, G.A., Churchland, A.K., Davatolhagh, M.F., Lee, H.D., Faulkner, M., Hu, F., Hunterberg, J., Khanal, A., Krasniak, C., Meijer, G.T., Miska, N.J., Mohammadi, Z., Noel, J.-P., Paninski, L., Pan-Vazquez, A., Roth, N., Schartner, M., Socha, K., Steinmetz, N.A., Svoboda, K., Taheri, M., Urai, A.E., Wells, M., West, S.J., Whiteway, M.R., Winter, O., Witten, I.B., 2022. Reproducibility of in-vivo electrophysiological measurements in mice. https://doi.org/10.1101/2022.05.09.491042

Inagaki, H.K., Chen, S., Daie, K., Finkelstein, A., Fontolan, L., Romani, S., Svoboda, K., 2022. Neural Algorithms and Circuits for Motor Planning. Annu. Rev. Neurosci. 45, 249–271. https://doi.org/10.1146/annurev-neuro-092021-121730

Jacobsen, K.R., Kalliokoski, O., Teilmann, A.C., Hau, J., Abelson, K.S.P., 2012. The effect of isoflurane anaesthesia and vasectomy on circulating corticosterone and ACTH in BALB/c mice. General and Comparative Endocrinology 179, 406–413. https://doi.org/10.1016/j.ygcen.2012.09.012

Juavinett, A.L., Bekheet, G., Churchland, A.K., 2019. Chronically implanted Neuropixels probes enable high-yield recordings in freely moving mice. eLife 8, e47188. https://doi.org/10.7554/eLife.47188

Juavinett, A.L., Nauhaus, I., Garrett, M.E., Zhuang, J., Callaway, E.M., 2017. Automated identification of mouse visual areas with intrinsic signal imaging. Nat Protoc 12, 32–43. https://doi.org/10.1038/nprot.2016.158

Jun, J.J., Steinmetz, N.A., Siegle, J.H., Denman, D.J., Bauza, M., Barbarits, B., Lee, A.K., Anastassiou, C.A., Andrei, A., Aydın, Ç., Barbic, M., Blanche, T.J., Bonin, V., Couto, J., Dutta, B., Gratiy, S.L., Gutnisky, D.A., Häusser, M., Karsh, B., Ledochowitsch, P., Lopez, C.M., Mitelut, C., Musa, S., Okun, M., Pachitariu, M., Putzeys, J., Rich, P.D., Rossant, C., Sun, W., Svoboda, K., Carandini, M., Harris, K.D., Koch, C., O'Keefe, J., Harris, T.D., 2017. Fully integrated silicon probes for high-density recording of neural activity. Nature 551, 232–236. https://doi.org/10.1038/nature24636

Jung, J.C., Mehta, A.D., Aksay, E., Stepnoski, R., Schnitzer, M.J., 2004. In Vivo Mammalian Brain Imaging Using One- and Two-Photon Fluorescence Microendoscopy. Journal of Neurophysiology 92, 3121–3133. https://doi.org/10.1152/jn.00234.2004

Kauvar, I.V., Machado, T.A., Yuen, E., Kochalka, J., Choi, M., Allen, W.E., Wetzstein, G., Deisseroth, K., 2020. Cortical Observation by Synchronous Multifocal Optical Sampling Reveals Widespread Population Encoding of Actions. Neuron 107, 351-367.e19. https://doi.org/10.1016/j.neuron.2020.04.023

Kim, T.H., Zhang, Y., Lecoq, J., Jung, J.C., Li, J., Zeng, H., Niell, C.M., Schnitzer, M.J., 2016. Long-Term Optical Access to an Estimated One Million Neurons in the Live Mouse Cortex. Cell Reports 17, 3385–3394. https://doi.org/10.1016/j.celrep.2016.12.004

Koralek, A.C., Costa, R.M., Carmena, J.M., 2013. Temporally Precise Cell-Specific Coherence Develops in Corticostriatal Networks during Learning. Neuron 79, 865–872. https://doi.org/10.1016/j.neuron.2013.06.047

Li, N., Chen, S., Guo, Z.V., Chen, H., Huo, Y., Inagaki, H.K., Chen, G., Davis, C., Hansel, D., Guo, C., Svoboda, K., 2019. Spatiotemporal constraints on optogenetic inactivation in cortical circuits. eLife 8, e48622. https://doi.org/10.7554/eLife.48622

Machado, T.A., Kauvar, I.V., Deisseroth, K., 2022. Multiregion neuronal activity: the forest and the trees. Nat Rev Neurosci 23, 683–704. https://doi.org/10.1038/s41583-022-00634-0

McBride, E.G., Gandhi, S.R., Kuyat, J.R., Ollerenshaw, D.R., Arkhipov, A., Koch, C., Olsen, S.R., 2023. Influence of claustrum on cortex varies by area, layer, and cell type. Neuron 111, 275-290.e5. https://doi.org/10.1016/j.neuron.2022.10.026

McKinney, M.M., Dupont, W.D., Corson, K.J., Wallace, J.M., Jones, C.P., 2022. Physiologic and Behavioral Effects in Mice Anesthetized with Isoflurane in a Red-tinted or a Traditional Translucent Chamber. J Am Assoc Lab Anim Sci 61, 322–332. https://doi.org/10.30802/AALAS-JAALAS-22-000011

Musall, S., Kaufman, M.T., Juavinett, A.L., Gluf, S., Churchland, A.K., 2019. Single-trial neural dynamics are dominated by richly varied movements. Nat Neurosci 22, 1677–1686. https://doi.org/10.1038/s41593-019-0502-4

Nestvogel, D.B., McCormick, D.A., 2022. Visual thalamocortical mechanisms of waking state-dependent activity and alpha oscillations. Neuron 110, 120-138.e4. https://doi.org/10.1016/j.neuron.2021.10.005

Nicolelis, M.A.L., Baccala, L.A., Lin, R.C.S., Chapin, J.K., 1995. Sensorimotor Encoding by Synchronous Neural Ensemble Activity at Multiple Levels of the Somatosensory System. Science 268, 1353–1358.

Oh, S.W., Harris, J.A., Ng, L., Winslow, B., Cain, N., Mihalas, S., Wang, Q., Lau, C., Kuan, L., Henry, A.M., Mortrud, M.T., Ouellette, B., Nguyen, T.N., Sorensen, S.A., Slaughterbeck, C.R., Wakeman, W., Li, Y., Feng, D., Ho, A., Nicholas, E., Hirokawa, K.E., Bohn, P., Joines, K.M., Peng, H., Hawrylycz, M.J., Phillips, J.W., Hohmann, J.G., Wohnoutka, P., Gerfen, C.R., Koch, C., Bernard, A., Dang, C., Jones, A.R., Zeng, H., 2014. A mesoscale connectome of the mouse brain. Nature 508, 207–214. https://doi.org/10.1038/nature13186

Pachitariu, M., Sridhar, S., Stringer, C., 2023. Solving the spike sorting problem with Kilosort. https://doi.org/10.1101/2023.01.07.523036

Peters, A.J., Fabre, J.M.J., Steinmetz, N.A., Harris, K.D., Carandini, M., 2021. Striatal activity topographically reflects cortical activity. Nature 591, 420–425. https://doi.org/10.1038/s41586-020-03166-8

Pfurtscheller, G., Stancak Jr, A., Neuper, C., 1996. Event-related synchronization (ERS) in the alpha band—an electrophysiological correlate of cortical idling: a review. International journal of psychophysiology 24, 39–46.

Reig, R., Silberberg, G., 2014. Multisensory Integration in the Mouse Striatum. Neuron 83, 1200–1212. https://doi.org/10.1016/j.neuron.2014.07.033

Ren, C., Komiyama, T., 2021. Characterizing Cortex-Wide Dynamics with Wide-Field Calcium Imaging. J. Neurosci. 41, 4160–4168. https://doi.org/10.1523/JNEUROSCI.3003-20.2021

Resulaj, A., Ruediger, S., Olsen, S.R., Scanziani, M., 2018. First spikes in visual cortex enable perceptual discrimination. eLife 7, e34044. https://doi.org/10.7554/eLife.34044

Romo, R., Salinas, E., 2003. Flutter Discrimination: neural codes, perception, memory and decision making. Nat Rev Neurosci 4, 203–218. https://doi.org/10.1038/nrn1058

Saalmann, Y.B., Pinsk, M.A., Wang, L., Li, X., Kastner, S., 2012. The Pulvinar Regulates Information Transmission Between Cortical Areas Based on Attention Demands. Science 337, 753–756. https://doi.org/10.1126/science.1223082

Senzai, Y., Fernandez-Ruiz, A., Buzsáki, G., 2019. Layer-Specific Physiological Features and Interlaminar Interactions in the Primary Visual Cortex of the Mouse. Neuron 101, 500-513.e5. https://doi.org/10.1016/j.neuron.2018.12.009

Siegle, J.H., Jia, X., Durand, S., Gale, S., Bennett, C., Graddis, N., Heller, G., Ramirez, T.K., Choi, H., Luviano, J.A., Groblewski, P.A., Ahmed, R., Arkhipov, A., Bernard, A., Billeh, Y.N., Brown, D., Buice, M.A., Cain, N., Caldejon, S., Casal, L., Cho, A., Chvilicek, M., Cox, T.C., Dai, K., Denman, D.J., de Vries, S.E.J., Dietzman, R., Esposito, L., Farrell, C., Feng, D., Galbraith, J., Garrett, M., Gelfand, E.C., Hancock, N., Harris, J.A., Howard, R., Hu, B., Hytnen, R., Iyer, R., Jessett, E., Johnson, K., Kato, I., Kiggins, J., Lambert, S., Lecoq, J., Ledochowitsch, P., Lee, J.H., Leon, A., Li, Y., Liang, E., Long, F., Mace, K., Melchior, J., Millman, D., Mollenkopf, T., Nayan, C., Ng, L., Ngo, K., Nguyen, T., Nicovich, P.R., North, K., Ocker, G.K., Ollerenshaw, D., Oliver, M., Pachitariu, M., Perkins, J., Reding, M., Reid, D., Robertson, M., Ronellenfitch, K., Seid, S., Slaughterbeck, C., Stoecklin, M., Sullivan, D., Sutton, B., Swapp, J., Thompson, C., Turner, K., Wakeman, W., Whitesell, J.D., Williams, D., Williford, A., Young, R., Zeng, H., Naylor, S., Phillips, J.W., Reid, R.C., Mihalas, S., Olsen, S.R., Koch, C., 2021. Survey of spiking in the mouse visual system reveals functional hierarchy. Nature 592, 86–92. https://doi.org/10.1038/s41586-020-03171-x

Siegle, J.H., López, A.C., Patel, Y.A., Abramov, K., Ohayon, S., Voigts, J., 2017. Open Ephys: an open-source, plugin-based platform for multichannel electrophysiology. J. Neural Eng. 14, 045003. https://doi.org/10.1088/1741-2552/aa5eea

Sofroniew, N.J., Flickinger, D., King, J., Svoboda, K., 2016. A large field of view two-photon mesoscope with subcellular resolution for in vivo imaging. eLife 5, e14472. https://doi.org/10.7554/eLife.14472

Steinmetz, N.A., Aydin, C., Lebedeva, A., Okun, M., Pachitariu, M., Bauza, M., Beau, M., Bhagat, J., Böhm, C., Broux, M., Chen, S., Colonell, J., Gardner, R.J., Karsh, B., Kloosterman, F., Kostadinov, D., Mora-Lopez, C., O'Callaghan, J., Park, J., Putzeys, J., Sauerbrei, B., van Daal, R.J.J., Vollan, A.Z., Wang, S., Welkenhuysen, M., Ye, Z., Dudman, J.T., Dutta, B., Hantman, A.W., Harris, K.D., Lee, A.K., Moser, E.I., O'Keefe, J., Renart, A., Svoboda, K., Häusser, M., Haesler, S., Carandini, M., Harris, T.D., 2021. Neuropixels 2.0: A miniaturized high-density probe for stable, long-term brain recordings. Science 372, eabf4588. https://doi.org/10.1126/science.abf4588

Steinmetz, N.A., Zatka-Haas, P., Carandini, M., Harris, K.D., 2019. Distributed coding of choice, action and engagement across the mouse brain. Nature 576, 266–273. https://doi.org/10.1038/s41586-019-1787-x

Stringer, C., Pachitariu, M., Steinmetz, N., Reddy, C.B., Carandini, M., Harris, K.D., 2019. Spontaneous behaviors drive multidimensional, brainwide activity. Science 364, eaav7893. https://doi.org/10.1126/science.aav7893

van Daal, R.J.J., Aydin, Ç., Michon, F., Aarts, A.A.A., Kraft, M., Kloosterman, F., Haesler, S., 2021. Implantation of Neuropixels probes for chronic recording of neuronal activity in freely behaving mice and rats. Nat Protoc 16, 3322–3347. https://doi.org/10.1038/s41596-021-00539-9

Vesuna, S., Kauvar, I.V., Richman, E., Gore, F., Oskotsky, T., Sava-Segal, C., Luo, L., Malenka, R.C., Henderson, J.M., Nuyujukian, P., Parvizi, J., Deisseroth, K., 2020. Deep posteromedial cortical rhythm in dissociation. Nature 586, 87–94. https://doi.org/10.1038/s41586-020-2731-9

Von Stein, A., Sarnthein, J., 2000. Different frequencies for different scales of cortical integration: from local gamma to long range alpha/theta synchronization. International journal of psychophysiology 38, 301–313.

Wekselblatt, J.B., Flister, E.D., Piscopo, D.M., Niell, C.M., 2016. Large-scale imaging of cortical dynamics during sensory perception and behavior. APSselect 3, 2852–2866. https://doi.org/10.1152/jn.01056.2015@apsselect.2016.3.issue-4

Yang, Z., Wang, K.K.W., 2015. Glial Fibrillary acidic protein: From intermediate filament assembly and gliosis to neurobiomarker. Trends Neurosci 38, 364–374. https://doi.org/10.1016/j.tins.2015.04.003

Zhao, S., Ting, J.T., Atallah, H.E., Qiu, L., Tan, J., Gloss, B., Augustine, G.J., Deisseroth, K., Luo, M., Graybiel, A.M., Feng, G., 2011. Cell type–specific channelrhodopsin-2 transgenic mice for optogenetic dissection of neural circuitry function. Nat Methods 8, 745–752. https://doi.org/10.1038/nmeth.1668

SUPPLEMENTAL FIGURES

A

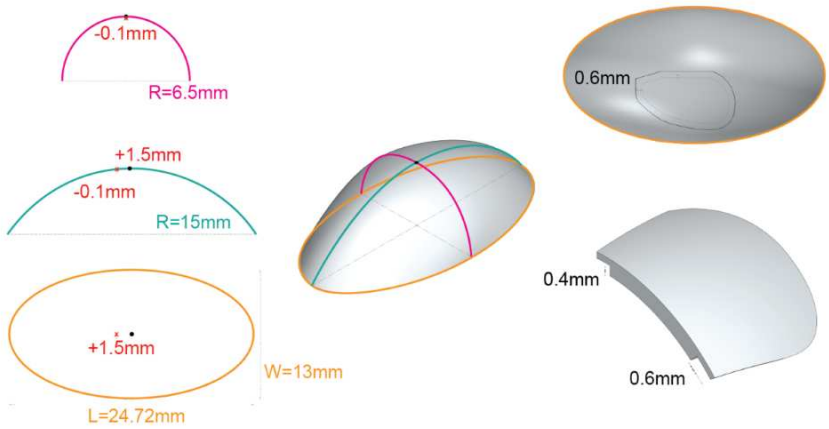

B

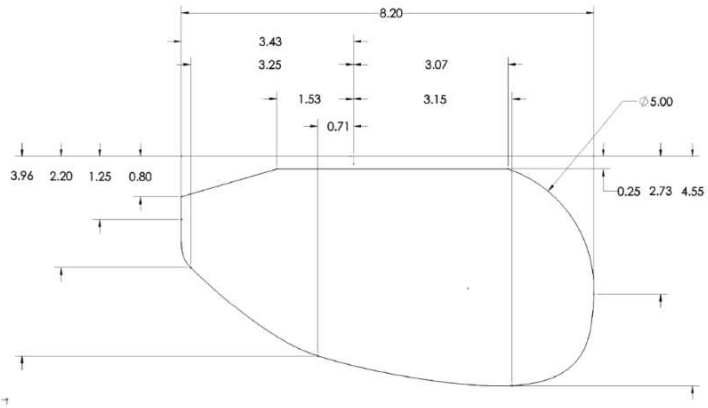

C

D

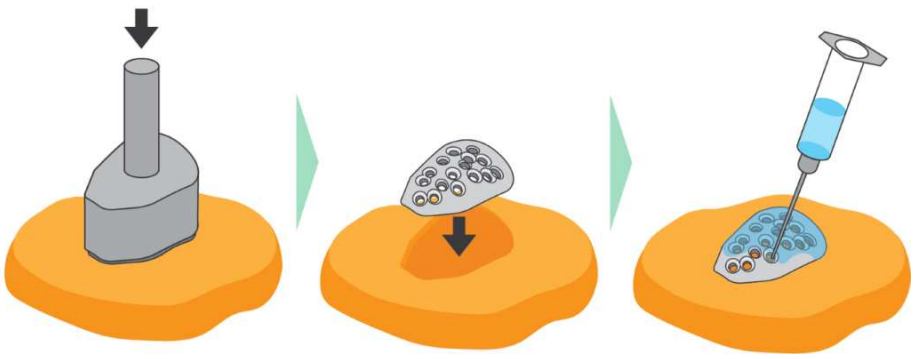

Figure S1. Implant creation and coating.

A) Using computer-aided design (CAD) software, the implant design was initially created as a triaxial ellipsoid-like surface intended to match the curvature of an average mouse skull in the area where the craniotomy is located (see Figure 2A). The surface is defined by three curves with respect to Bregma (red x). The shape of the implant is cut out of the ellipsoid surface. The lip of the implant was set at 0.6mm and stump set at 0.4mm. **B)** Top-down (X and Y) dimensions (in mm) of the implant. **C)** Implant holes are created over target coordinates at an angle that matches Neuropixels probe insertion angles. Each hole receives 45-degree chamfers, allowing for some flexibility in probe insertion angles. Implants are then 3D-printed in clear resin at the orientation shown, UV cured at 60C for 15min, and rinsed with isopropyl alcohol prior to storage. **D)** Coating implants with SORTA-Clear requires making an impression of the implant in putty using a custom stamp tool. The implant is then gently placed into the impression. SORTA-Clear is loaded into a 1mL syringe with 25g needle and each hole is slowly filled to prevent air from getting trapped. After filling each hole, the entire surface of the implant is covered with a thin layer leaving the lip portion at the edges uncovered. Coated implants are allowed to cure for 24h before being removed from putty. They are then rinsed with 70% EtOH, dried, and individually packaged for the autoclave.

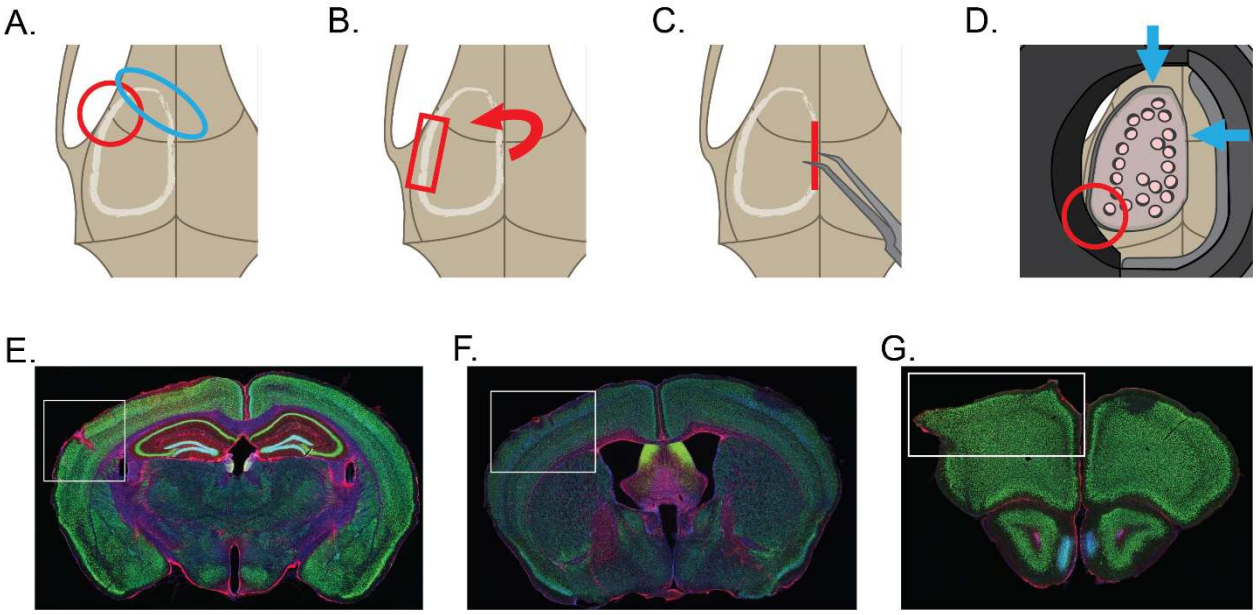

Figure S2. Surgical tips and troubleshooting.

A) The drilling depth in the upper left corner of the craniotomy can vary substantially due to small variations in proximity to the eye socket (red). The drill path comes very close to the rostral rhinal vein and heavy vasculature near its intersection with the sagittal sinus (blue). **B)** While it is advised to drill until a crack or separation occurs over most of the drill path, it is often helpful to leave a very thin layer of bone on the lateral edge (red rectangle) of the craniotomy to act as a hinge when removing the skull. **C)** Begin removal of the drilled skull from the medial side. **D)** When placing the implant, align it to the anterior and medial edges (blue arrows) to

ensure accurate placement, as the lateral edge is more difficult to visualize. Clearance between the well, metabond, and implant can be very tight in the lower lefthand corner, so care should be taken to keep the metabond low enough to account for the curvature of the implant lip (red circle). **E-G).** Histological examples of tissue damage caused by excessive drilling (E), dura tearing during durotomy (F), and improper seating of the implant in the craniotomy (G).

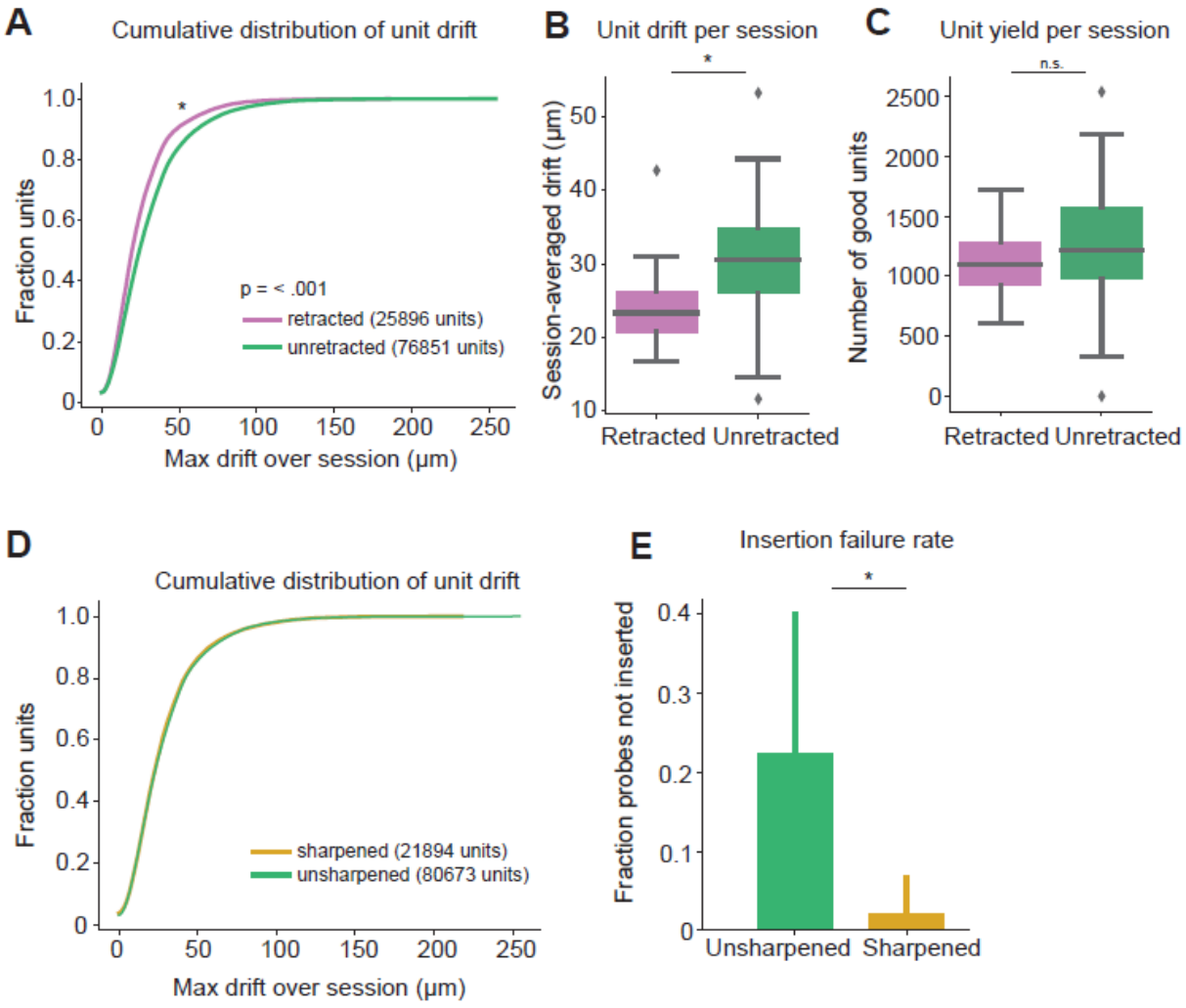

Figure S3. Neuropixels Probe Troubleshooting.
A) Retracting Neuropixels probes 100μm after inserting reduces unit drift. Cumulative distribution of point-to-point drift over session per unit with (pink, n = 25,896 units) and without (green, n = 76,851) probe retraction. Probes were retracted on a session-by-session basis. Units from sessions where probes were retracted had lower drift (mean = 24.48 μm) than those from sessions where probes were not retracted (mean = 30.25 μm; Kolmogrov-Smirnov test, p < .001). **B)** Sessions in which Neuropixels probes were retracted show less drift on average. Shown is point to point drift averaged across all units recorded in each session. Average drift within retracted sessions (n = 23, mean = 24.23 μm) was less than non-retracted sessions (n = 60, mean = 30.56 μm). **C)** Number of good units recorded per session is similar across

retracted and non-retracted sessions. Histogram showing distribution of unit yield for retracted (mean = 1125 units) and non-retracted (mean = 1280 units) sessions. Distributions did not differ significantly (Kolmogrov-Smirnov test, p = .318). **D)** Sharpened Neuropixels probes show comparable drift to unsharpened probes. Cumulative distribution of point-to-point drift over session per unit with (yellow, n = 21,894 units) and without (green, n = 80,673) sharpened probe tips. **E)** We sharpened 2 of 6 Neuropixels probe tips during data collection. Insertion failure rate for those probes before sharpening (green, n=32 insertions) and after sharpening (gold, n=112) is shown with 95% confidence intervals (binomial test). Sharpened Neuropixels probes have a lower insertion fail rate than unsharpened probes (p = .0004, Fisher's exact test).

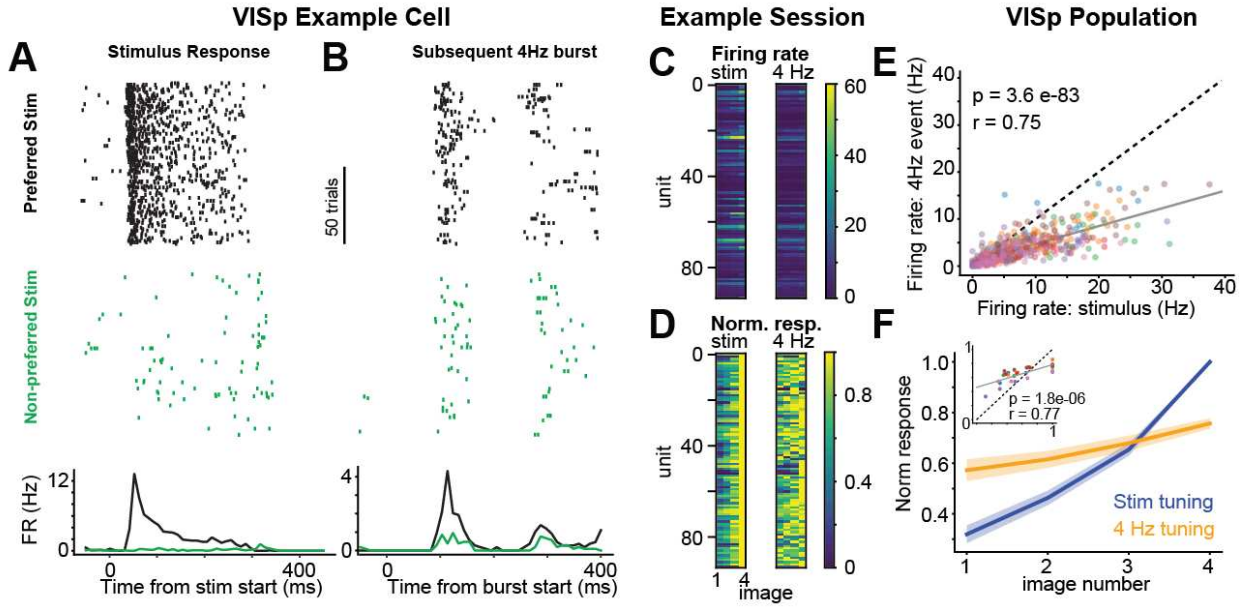

Figure S4. Replay of recent sensory activation during alpha events in VISp.
A) Spike raster for one example VISp unit during presentation of a preferred natural image (top, black) and a non-preferred image (green). (Bottom) PSTH of same unit for preferred and non-preferred image presentations. The image was presented for 250 ms starting at time zero. **B)** Raster of same unit for alpha burst events following stimulus presentation trials in (A). Note that this unit responds more vigorously following presentation of its preferred stimulus. **C)** (Left) Heatmap showing tuning of all VISp units recorded during an example experiment for the four stimuli presented during the session. Rows depict the mean response for individual units to each of the four stimuli shown during this session sorted by magnitude. (Right) Heatmap showing response of same units to the alpha burst event following visual stimulation. For each unit, the order of the row elements is the same as (C). **D)** Same as (C) but row normalized. **E)** Correlation of firing rate during visual stimulation and subsequent alpha burst. Each dot is a VISp unit, color-coded by recording session. **F)** Mean stimulus tuning across all VISp units for the sensory-evoked response (blue) and the subsequent alpha burst (orange). This plot is the column average of (D) but across all recording sessions.